Wave power absorption by an oscillating water column (OWC) device of annular cross-section in a combined wind-wave energy system

Cong, Peiwen
State Key Laboratory of Coastal and Offshore Engineering, Dalian University of Technology

Teng, Bin
State Key Laboratory of Coastal and Offshore Engineering, Dalian University of Technology

Bai, Wei
Department of Computing and Mathematics, Manchester Metropolitan University

Ning, Dezhi
State Key Laboratory of Coastal and Offshore Engineering, Dalian University of Technology

他

出版情報：Applied Ocean Research. 107 (102499), 2021-02. Elsevier
バージョン：
権利関係：

Manuscript:

Wave power absorption by an oscillating water column (OWC) device of annular cross-section in a combined wind-wave energy system

Peiwen Cong[a], Bin Teng[a], Wei Bai[b], Dezhi Ning[a], and Yingyi Liu[c]

[a] State Key Laboratory of Coastal and Offshore Engineering, Dalian University of Technology, Dalian 116024, China

[b] Department of Computing and Mathematics, Manchester Metropolitan University, Chester Street, Manchester M1 5GD, UK

[c] Research Institute for Applied Mechanics, Kyushu University, Fukuoka 8168580, Japan

Abstract

This paper deals with a new combined concept consisting of an oscillating water column (OWC) device and an offshore wind turbine for the multi-purpose utilization of offshore renewable energy resources. The wind turbine is supported by a monopile foundation, and the attached OWC is coaxial with the foundation. Within the chamber, four vertical stiffening plates connect the exterior shell of the OWC and the monopile foundation. Correspondingly, the whole chamber is divided into four equivalent fan-shaped sub-chambers. A higher-order boundary element method is then adopted to model the wave interaction with the combined system. Numerical models based on two different approaches, namely 'Direct' and 'Indirect', are both developed in this study. In addition, a self-adaptive Gauss integration method is developed to treat the nearly singular integration that occurs when the field and source points are very close to each other. A detailed numerical analysis is then conducted for the case of an OWC integrated into a NREL 5 MW wind turbine in both regular and irregular sea states. Numerical results illustrate that a significant energy extraction efficiency is attained

when remarkable piston-like fluid motion is induced within each sub-chamber, and the wave power absorption by the OWC is not restricted by the wave direction. The air compressibility makes a negative effect on the wave power absorption especially when the wave frequency is less than the resonance frequency of the piston-mode motion of the fluid in the chamber. In addition, the wave forces on the OWC and the monopile can balance each other at specific wave conditions, leading to a nearly zero net wave force on the whole system. The results also illustrate that by using an optimal turbine parameter, the wave power production by the OWC can be an important supplement to the combined system in operational sea states.

Keywords: combined concept; wind turbine; monopile foundation; oscillating water column (OWC); HOBEM

1. Introduction

The ocean is vast and powerful, enabling marine renewable energy to be potentially a significant energy supply. Due to the high power density and longtime availability, considerable efforts and advances have been made in exploiting the power of ocean waves worldwide, and a variety of wave energy converters have been invented to harvest the wave energy. Among different classes of designs, the oscillating water column (OWC) device has been widely regarded as one of the most promising options [1]. A typical OWC device mainly consists of a collector chamber with an underwater bottom open to the sea and a power take-off (PTO) system, mostly an air turbine, on the roof of the chamber [2]. In addition, in a typical OWC, the moving mechanical part is only the air turbine, located above the water surface. Due to the nature of simplicity, the OWC is flexibly adapted to the shoreline, nearshore, and offshore through different forms.

In the case of an onshore OWC, the wet power-transmission cables and mooring lines are not required. In addition, onshore OWCs can be easily maintained and normally operate in safe sea environments, which increases their survivability. Due to the

apparent advantages, onshore OWCs have attracted much attention from researchers, and there have been many attempts on the hydrodynamic aspects of onshore OWCs [3–7]. As the waves approach the shore, a considerable amount of wave energy can be consumed due to the bottom friction. In addition, the shoreline location introduces limitation to the deployment of large numbers of devices. Therefore, offshore OWCs, which can be exposed to a higher amount of wave energy, have also been suggested and designed by many researchers [8–10]. Offshore OWCs are in general floating devices, with a typical geometry consisting of a truncated vertical column with an open bottom. Regarding random ocean waves, broadening the effective frequency bandwidth of an OWC device is of great importance for its adaption to variable ocean environments. Therefore, researchers [11-17] have reported innovative configurations of the OWC device, such as dual-chamber OWCs and OWC arrays. In the meantime, as the cost sharing between the energy extraction and coastal protection can help improve the economic viability, the idea of the integration of an OWC device into a breakwater has also been proposed by researchers, such as [18–20].

In addition to wave energy, wind energy is also a great source of renewable energy. Wind energy converters have been used for the harvesting and exploitation of the available enormous wind energy resources. Offshore wind turbine technology has been being developed rapidly in recent years, and it can be considered as the leading technology in the offshore renewable energy sector. For both the offshore wind turbine and the wave energy converter, there is a need for a reduction in the cost and the further development. Due to the natural correlation, wave energy may also be of considerable amount where the offshore wind energy resource is rich. Significant opportunities and benefits have been identified through an integration of the energy systems of different technologies into one single platform. The combination of the wind and wave energy devices can reduce the cost relevant to the operation and maintenance, foundation substructure as well as the required electric grid infrastructure especially with regard to the transportation of the produced power to onshore stations [21]. Except for the good aspects from a cost-benefit point of view, the combination of the two energy systems can also lead to the efficient use of the ocean space [22]. Due to the various possible

advantages as a result of the combination of the wind and wave energy converters, several concepts of the combined system have been proposed, and the concept feasibility of different integrated platforms has been assessed. Examples include the integration of a point-absorber-type wave energy converter with a semisubmersible type or a spar type wind turbine [21, 23–25]; integration of an OWC with a floating or bottom-mounted offshore wind turbine [26–31], and semisubmersible flap concept [22, 32–33].

So far, the most widely used support structure for an offshore wind turbine is the monopile foundation, accounting for 87% of the installed wind farms in Europe [34]. In the meantime, among various wave energy converters, the OWC device has been considered as one of the most promising options, reaching the stage of full-scale prototypes. It suggests that the integration of an OWC with a monopile supporting a wind turbine can be a promising solution for the multi-purpose utilization of offshore renewable energy. For structures of fundamental geometry, analytical solutions can be achieved. An analytical solution has been developed in [29] for a combined wind-wave energy system, in which the exterior shell of the attached OWC has a skirt whose scope is to guide the wave energy flux inside the chamber. In the meantime, for structures of complex geometry, it is quite difficult to achieve analytical solutions. Then, a numerical approach has to be developed. In this study, a novel combined concept consisting of an oscillating water column (OWC) device and an offshore wind turbine is proposed. As shown Fig. 1, the wind turbine is supported by a monopile foundation, and the OWC is coaxial with the foundation. The OWC is partly submerged with its bottom open to the sea. An air duct, which houses an air turbine, is installed on the roof of the chamber. Within the chamber, the exterior shell of the OWC and the monopile foundation are connected by four vertical stiffening plates. Correspondingly, the whole chamber is divided into four fan-shaped sub-chambers. The performance of the proposed system is then investigated. In order to achieve this, numerical models based on HOBEM are developed to analyze the wave interaction with the combined system. Based on the developed models, a detailed numerical study is then conducted, and the wave power absorption by the combined system in both regular and irregular sea states are analyzed.

120 The remaining part of the paper is organized as follows. First, the hydrodynamic
121 problem and the power take-off model is introduced. In the next section, a solution to
122 the boundary value problem is developed, which is followed by the calculation of the
123 volume flux, air pressure, optimal pneumatic damping coefficient, and wave power
124 absorption. Then, after examining the convergence and validity of the proposed model,
125 a detailed numerical analysis is conducted. Finally, conclusions are drawn based on the
126 previous analysis.

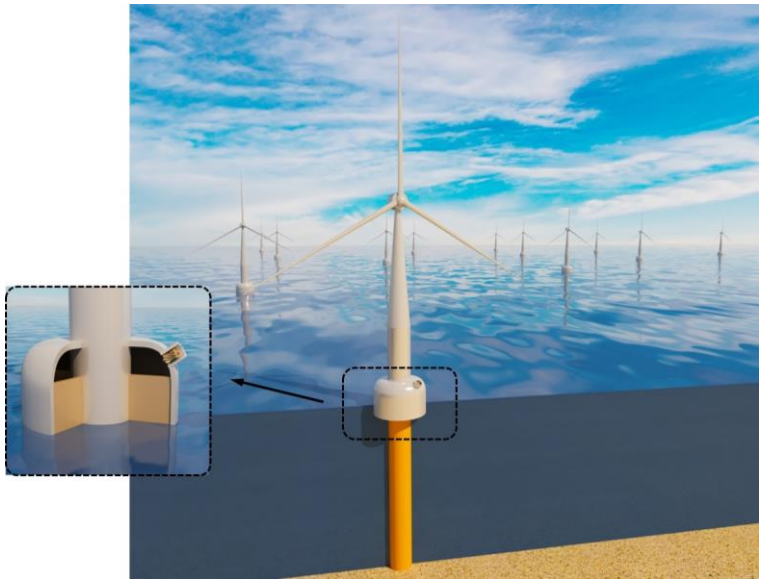

127

128 Fig. 1 Overview of a combined concept consisting of a monopile wind turbine and an attached
129 OWC device

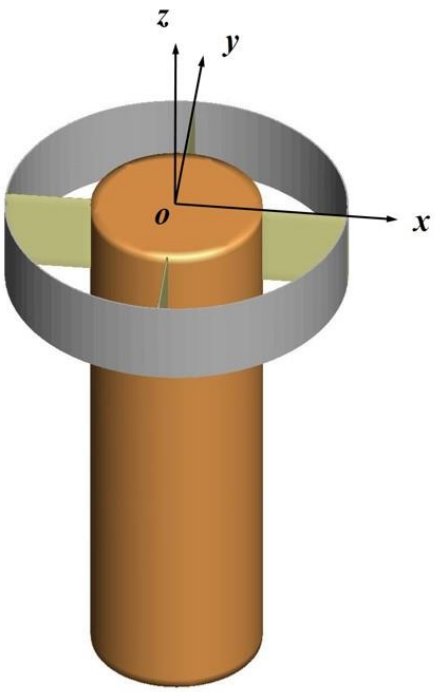

130

Fig. 2 Definition of the coordinate system

2. Description of the hydrodynamic problem and the power take-off model

The hydrodynamic performance of a combined concept consisting of an OWC device and an offshore wind turbine is considered. As shown in Fig. 1, the monopile is of radius a, and the OWC is made coaxial with the monopile. Then, the monopile plays the role of the interior shell of the OWC. The draft of the OWC is d. For the exterior shell of the OWC, its inner and outer radii are R_i and R_e, respectively, with $e = R_e - R_i$ being the thickness of the exterior shell. The chamber is connected with the external atmosphere by a duct installed on the roof of the chamber, and there exists an air turbine housed in the duct. Within the chamber, the exterior shell of the OWC and the monopile foundation are connected by four vertical stiffening plates. The plates are with the thickness e and draft d. The whole chamber of the OWC is then divided into four fan-shaped sub-chambers. At initial time, the free surfaces inside and outside the chamber are at the same level, and there is an amount of air entrapped above the water surface inside the chamber. The definition of the Cartesian and cylindrical coordinate systems is given in Fig. 2. The oxy and $or\theta$ planes are both located on the mean plane of the free surface, and the z-axis is oriented vertically upward. $r = \sqrt{x^2 + y^2}$ and $\theta = \tan^{-1}(y/x)$. Two plates are installed along the x-axis, and the other two are along the y-axis. The water depth h is a constant in this study.

It is assumed that the fluid is inviscid and incompressible with a constant density ρ, the fluid motion is irrotational, and the wave steepness is small. The linear potential flow theory can then be used, and there exists a velocity potential $\Phi(\boldsymbol{x}; t)$ satisfying the Laplace's equation in the fluid domain. That is

$$\nabla^2\Phi(\mathbf{x}; t) = 0. \tag{1}$$

The combined system is exposed to the action of a plane incident wave of amplitude A, and frequency ω. The wave heading is β with respect to the positive x-direction. A frequency-domain analysis is conducted, and all time-dependent variables are assumed

to be harmonic. The time factor can then be separated, and the velocity potential will have the following form

$$\Phi(\mathbf{x};\, t) = \mathrm{Re}\left[\phi^{(1)}(\mathbf{x})e^{-i\omega t}\right], \tag{2}$$

in which 'Re' is the real part of a complex variable; $i = \sqrt{-1}$.

Besides Laplace's equation, the velocity potential must satisfy appropriate boundary conditions. On the exterior free surface S_e ($r \geq R_e$), there is only the atmospheric pressure P_0. However, the inner free surface S_i ($a \leq r \leq R_i$) is subjected to an air pressure distribution of $P_0 + P_c(t)$, in which $P_c(t)$ is the oscillating air pressure. Due to the high sound speed in air and the low frequency of ocean waves, the oscillating air pressure can be considered spatially uniform throughout the whole chamber [19]. Referring to [35], after assuming isentropy and using a linear wave theory, the mass flux of the air through a linear turbine is related to the oscillating air pressure by

$$\frac{\mathrm{d}M_a}{\mathrm{d}t} = \rho_a Q_c - \frac{V_0}{c^2}\frac{\mathrm{d}P_c}{\mathrm{d}t} = \frac{KD}{N}P_c, \tag{3}$$

in which M_a is the mass of the air in the chamber; Q_c is the change rate of the total volume of air inside the chamber; V_0 is the air volume in the chamber in calm water; ρ_a is the air density; D is the diameter of the turbine rotor; N is the speed of the turbine rotation; c is the speed of the sound in air; K is an empirical coefficient depending on the design of the turbines [19]. For simple harmonic motions with

$$Q_c(t) = \mathrm{Re}\left[q_c e^{-i\omega t}\right]; \tag{4a}$$

$$P_c(t) = \mathrm{Re}\left[p_c e^{-i\omega t}\right], \tag{4b}$$

we can have

$$q_c = \Lambda p_c, \tag{5}$$

in which q_c and p_c are the amplitudes of the volume flux and the oscillating air pressure, respectively. The parameter Λ is expressed as

$$\Lambda = \chi - i\omega\mu, \tag{6}$$

with

$$\chi = \frac{KD}{N\rho_a}; \tag{7a}$$

$$\mu = \frac{V_0}{c^2\rho_a}. \tag{7b}$$

χ depends on the design of the air turbine, and can be adjusted by some ways, such as varying the rotational speed N. μ represents the effect of compressibility of air in the chamber, and is analogous to a spring constant [19]. The compressibility of air in a chamber with a larger size can be more evident as discussed in Sheng et al. [36]. Hereinafter, we define χ and μ as the turbine parameter and the chamber parameter, respectively.

In the hydrodynamic analysis, the effect of the oscillating air pressure should be considered properly. Then, on the mean plane of the free surface ($z = 0$), the combined kinematic and dynamic boundary condition is given by

$$\frac{\partial\phi}{\partial z} - \frac{\omega^2}{g}\phi = \frac{i\omega}{\rho g}p_c, \quad \text{on } S_i; \tag{8a}$$

$$\frac{\partial\phi}{\partial z} - \frac{\omega^2}{g}\phi = 0, \quad \text{on } S_e. \tag{8b}$$

On the mean wet surface of the combined system S_b, the boundary condition is given by

$$\frac{\partial\phi}{\partial n} = 0, \quad \text{on } S_b, \tag{9}$$

in which $\mathbf{n}$ is the normal unit vector pointing outward from the fluid domain. In the same way, the boundary condition on the impermeable sea bed ($z = -h$) is

$$\frac{\partial\phi}{\partial z} = 0, \quad \text{on } z = -h. \tag{10}$$

To ensure the uniqueness of the solution, ϕ has to satisfy the Sommerfeld radiation condition at a substantial distance from the structure. That is

$$\lim_{r\to\infty}\sqrt{r}\left[\frac{\partial}{\partial r}(\phi - \phi_I) - i\kappa_0(\phi - \phi_I)\right] = 0, \tag{11}$$

in which $\phi_I(\mathbf{x})$ represents the incident velocity potential, and it is given by

$$\phi_I(\mathbf{x}) = -\frac{iAg}{\omega}\frac{\cosh\kappa_0(z+h)}{\cosh\kappa_0 h}e^{i\kappa_0(x\cos\beta + y\sin\beta)}, \tag{12}$$

in which κ_0 is the wavenumber. κ_0 and ω satisfy the relationship $\omega^2 = g\kappa_0 \tanh \kappa_0 h$, with g being the gravitational acceleration.

The captured power W_c is the time-averaged rate of work done by the oscillating air pressure pushing the air through the air turbine [8]. W_c can be evaluated according to

$$W_c = \lim_{\hat{T}\to\infty}\left\{\frac{1}{\hat{T}}\int_t^{t+\hat{T}} P_c(t)Q_c(t)dt\right\}. \tag{13}$$

For regular incident wave, W_c can be further expressed as

$$W_c = \frac{1}{2}\mathrm{Re}\left[p_c q_c^*\right] = \frac{1}{2}\mathrm{Re}[\Lambda]|p_c|^2. \tag{14}$$

Following [37], the wave energy extraction efficiency E_c (also known as the relative capture width) for the present combined system is defined as

$$E_c = \frac{W_c}{W_{in}} = \frac{W_c}{2(R_i - a)P_{in}}, \tag{15}$$

in which W_{in} is the wave power of the free incident wave passing through the width of $2(R_i - a)$ over a wave period; P_{in}, representing the power flux density of the incident wave, is determined according to

$$P_{in} = \frac{1}{2}\rho g A^2 C_g. \tag{16}$$

In Eq. (16), C_g is the group velocity of the incident wave.

3. Numerical approach to the boundary value problem

In order to achieve a solution to the boundary value problem defined in the previous sections, a decomposition of the volume flux is made. The volume flux inside the chamber is then expressed as a sum of two distinct parts. That is

$$q_c = q_D - \frac{i\omega}{\rho g} p_c q_R, \tag{17}$$

in which q_D and q_R represent the volume flux due to a wave diffraction problem and a pressure-dependent wave radiation problem, respectively. Correspondingly, the velocity potential is divided into two parts. That is

$$\phi = \hat{\phi} - \frac{i\omega}{\rho g} p_c \phi_R. \tag{18}$$

In Eq. (18), $\hat{\phi}$ is a summation of the incident potential ϕ_I and the diffraction potential ϕ_D, i.e.

$$\hat{\phi} = \phi_I + \phi_D; \tag{19}$$

ϕ_R is a pressure-dependent radiation potential.

The wave diffraction is caused by the excitation of the incident wave when the air pressure inside and outside the chamber keeps the atmospheric pressure. The wave radiation occurs when the wave motion is purely due to the oscillating air pressure inside the chamber. The two problems can be regarded as the limited cases of the problem discussed in the previous section without the effect of the oscillating air pressure and the incident wave, respectively. ϕ_D and ϕ_R both satisfy the Laplace's equation, a no-flow condition on the seabed, as well as a Sommerfeld condition in the far field. On the free surface, the following conditions are held by ϕ_D and ϕ_R.

$$\frac{\partial \phi_D}{\partial z} - \frac{\omega^2}{g}\phi_D = 0, \quad \text{on } S_i \text{ and } S_e, \tag{20}$$

and

$$\frac{\partial \phi_R}{\partial z} - \frac{\omega^2}{g}\phi_R = \begin{cases} -1, & \text{on } S_i; \\ 0, & \text{on } S_e. \end{cases} \tag{21}$$

On the body surface, ϕ_D and ϕ_R satisfy the following boundary conditions

$$\frac{\partial \phi_D}{\partial n} = -\frac{\partial \phi_I}{\partial n}, \quad \text{on } S_b; \tag{22a}$$

$$\frac{\partial \phi_R}{\partial n} = 0, \quad \text{on } S_b. \tag{22b}$$

A boundary integral equation method is then used to solve the established boundary value problem, as it explicitly takes advantage of reducing the dimension of the problem by one order. The oscillating source, which satisfies a linear free-surface boundary condition, a no-flow condition on the horizontal seabed, and a Sommerfeld radiation condition at infinity, is used as Green's function. A mathematical expression for the Green's function $G(\mathbf{x}, \mathbf{x}_0; \omega)$ is given as follows

$$G(\mathbf{x}, \mathbf{x}_0; \omega) = -\frac{1}{4\pi}\left(\frac{1}{r_1} + \frac{1}{r_2}\right) + \frac{1}{4\pi}\int_0^\infty \frac{2(\nu+\mu)e^{-\mu h}\cosh\mu(z+h)\cosh\mu(z_0+h)}{\nu\cosh\nu h - \mu\sinh\mu h} J_0(\mu R)\, d\mu,$$

259 (23)

260 in which

261 $$R=\sqrt{\left(x-x_0\right)^2+\left(y-y_0\right)^2}; \tag{24a}$$

262 $$r_1=\sqrt{R^2+\left(z-z_0\right)^2}; \tag{24b}$$

263 $$r_2=\sqrt{R^2+\left(z+z_0+2d\right)^2}. \tag{24c}$$

264 In above equations, $\mathbf{x}$ and $\mathbf{x}_0$ are the field and source points, respectively; $J_0(\cdot)$ is the
265 Bessel function of zeroth order; $\nu=\omega^2/g$ is the deep-water wave number.

266 The use of the Green's second identity to the velocity potential and Green's function
267 can lead to a Fredholm integral equation of the second kind for ϕ_D and ϕ_R. Then, the
268 resulting boundary-integral equations for ϕ_D and ϕ_R are expressed as follows

269 $$\alpha\phi_D\left(\mathbf{x}_0\right)-\iint_{S_b}\frac{\partial G\left(\mathbf{x},\ \mathbf{x}_0;\ \omega\right)}{\partial n}\phi_D\left(\mathbf{x}\right)ds=\iint_{S_b}G\left(\mathbf{x},\ \mathbf{x}_0;\ \omega\right)\frac{\partial\phi_I}{\partial n}ds, \tag{25}$$

270 and

271 $$\alpha\phi_R\left(\mathbf{x}_0\right)-\iint_{S_b}\frac{\partial G\left(\mathbf{x},\ \mathbf{x}_0;\ \omega\right)}{\partial n}\phi_R\left(\mathbf{x}\right)ds=\iint_{S_i}G\left(\mathbf{x},\ \mathbf{x}_0;\ \omega\right)ds, \tag{26}$$

272 in which α is a measure of the normalized solid angle, and depends on the local shape
273 of the boundary surface. When $\mathbf{x}_0$ is on S_i, α is equal to unity. When $\mathbf{x}_0$ is on S_b, the
274 difficulty associated with the evaluation of α is overcome by formulating a
275 complementary problem within the interior of S_b. The higher-order boundary element
276 method (Teng and Eatock Taylor [38]) is used to solve Eqs. (25) and (26). Unknowns
277 on the body surface S_b as well as the inner free surface S_i are involved in the equations.
278 $\mathbf{x}_0$ is put on the body surface S_b as well as the inner free surface S_i, and S_b and S_i are
279 discretized into a set of curved quadrilateral or triangular elements.

280 As thin plates are installed within the chamber, the field point and source points are
281 close to each other at some conditions, leading to a nearly singular integration when
282 using the boundary element method. In order to overcome this difficulty, a self-adaptive
283 Gauss integration method is developed in this study. Following this method, when the
284 integration is conducted within a certain element and a nearly singular integration

happens, this element will be divided into a series of finer elements with a smaller size. The subdivision will not stop until the characteristic size of the sub-elements is equal to or smaller than the distance between the source and field points. As a result, the integral in the original element is transformed into that in the sub-elements with more Gauss points. Then, after using the isoperimetric techniques, the established boundary integral equations can be transformed into a system of linear algebraic equations, and solved by standard matrix techniques.

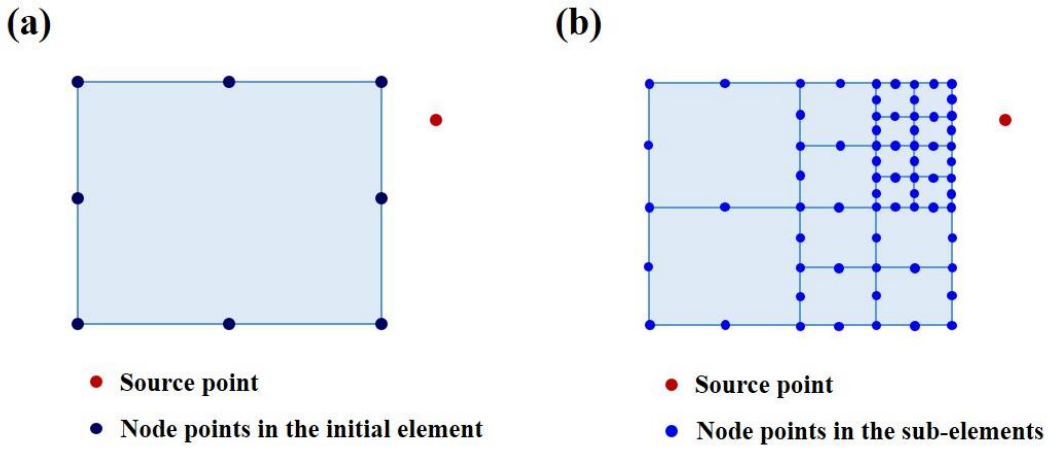

Fig. 3 Element subdivision based on a self-adaptive Gauss integration method: (a) Initial element, and (b) Sub-elements after subdivision

4. Calculation of the volume flux, air pressure, wave power absorption, and wave exciting force

Once the solution is obtained for the velocity potential, other physical quantities of interest can immediately be determined. Following Martins-Rivas and Mei [19], the volume flux in the wave diffraction and radiation problems can be calculated according to

$$q_D = \iint_{S_i} \frac{\partial \hat{\phi}}{\partial z} ds; \tag{27a}$$

$$q_R = \iint_{S_i} \frac{\partial \phi_R}{\partial z} ds. \tag{27b}$$

With the solution of q_D, the amplitudes of the total volume flux and the oscillating air

pressure can be evaluated according to the following expressions

$$q_c = \frac{\rho g \Lambda}{\rho g \Lambda + i\omega q_R} q_D; \tag{28a}$$

$$p_c = \frac{\rho g}{\rho g \Lambda + i\omega q_R} q_D. \tag{28b}$$

In addition, based on the kinematic conditions on the free surface, the surface elevation amplitude, which is denoted by η, is expressed as

$$\eta = -\frac{1}{i\omega}\frac{\partial \phi}{\partial z}\bigg|_{z=0} = -\frac{1}{i\omega}\left(\frac{\partial \phi_I}{\partial z} + \frac{\partial \phi_D}{\partial z} - \frac{i\omega}{\rho g} p_c \frac{\partial \phi_R}{\partial z}\right)\bigg|_{z=0}. \tag{29}$$

Following Falnes and Mciver [39], a decomposition of q_R is then made

$$-\frac{i\omega}{\rho g} q_R = -\left(C_b - iC_a\right). \tag{30}$$

Analogous to the electric circuit theory, $C_b - iC_a$ was defined as the radiation admittance in Evans and Porter [8] with C_a the radiation susceptance and C_b the radiation conductance. After inserting Eqs. (17) and (30) into Eq. (5), the following relationship is obtained

$$\left[\left(\chi - i\omega\mu\right) - \left(-C_b + iC_a\right)\right] p_c = q_D. \tag{31}$$

The power captured by the air turbine becomes

$$W_c = \frac{1}{2}\chi \frac{|q_D|^2}{\left(\chi + C_b\right)^2 + \left(\omega\mu + C_a\right)^2}. \tag{32}$$

For given wave conditions, the optimum extraction efficiency can be achieved by varying turbine parameter χ, the chamber parameter μ, or both. The chamber size and the monopile geometry cannot be easily adjusted. Hence, μ cannot be optimized for a broad range of wave conditions. As did in Martins-Rivas and Mei [19], we change the power-take off system (i.e., the parameter χ) to achieve the maximum energy extraction efficiency for given dimensions of an air chamber. χ can be adjusted by some ways, such as varying the angular velocity of the turbine rotor or controlling the pitch angle of the turbine blades. Then, we differentiate Eq. (32) only with respect to χ to obtain the following condition for a maximum wave power absorption

$$\hat{\chi}_{opt} = \sqrt{C_b^2 + \left(\omega\mu + C_a\right)^2}. \tag{33}$$

The use of Eqs. (15) and (32) gives

$$W_{c,\max} = \frac{1}{2}\frac{\sqrt{C_b^2 + (\omega\mu + C_a)^2}\,|q_D|^2}{\left[\sqrt{C_b^2 + (\omega\mu + C_a)^2} + C_b\right]^2 + (\omega\mu + C_a)^2}, \tag{34}$$

and

$$E_{c,\max} = \frac{1}{4(R_i - a)P_{in}}\frac{\sqrt{C_b^2 + (\omega\mu + C_a)^2}\,|q_D|^2}{\left[\sqrt{C_b^2 + (\omega\mu + C_a)^2} + C_b\right]^2 + (\omega\mu + C_a)^2}. \tag{35}$$

If we neglect the effect of the air compressibility and assume that there is no phase difference between the mass flux and the oscillating air pressure (i.e., $\mu = 0$), Eqs. (34) and (35) are reduced to

$$W_{c,\max} = \frac{1}{4}\frac{|q_D|^2}{\sqrt{C_a^2 + C_b^2} + C_b}, \tag{36}$$

and

$$E_{c,\max} = \frac{1}{8(R_i - a)P_{in}}\frac{|q_D|^2}{\sqrt{C_a^2 + C_b^2} + C_b}, \tag{37}$$

which are essential the same as the derivation in Evans and Porter [8].

After obtaining the velocity potential, the calculation of the wave force can be achieved by an integration of the wave pressure over the body surface. Then, we can have

$$\mathbf{f} = i\omega\rho\iint_{S_b}\left(\phi_I + \phi_D - \frac{i\omega}{\rho g}p_c\phi_R\right)\mathbf{n}ds. \tag{38}$$

5. Convergence test and validation

Numerical analysis is then conducted to assess the hydrodynamic performance of the combined concept. In the present study, we use $\rho = 1.025\times10^3$ kg/m^3, $\rho_a = 1.293$ kg/m^3, $g = 9.807$ m/s^2, and $c = 340$ m/s, respectively. In addition, the case of an annular OWC integrated into a NREL 5 MW wind turbine (Jonkman et al. [40]) is concerned. For this wind turbine, the mass of the blades as well as the nacelle is 3.5×10^5 kg, the mass of the tower is 3.4746×10^5 kg, and the radius of the monopile foundation is 3 m (i.e. $a = 3$ m).

In addition, the height of the air volume in calm water (denoted by h_0) are fixed at h_0 = 3.0 m in the subsequent calculation. Then, the air volume in calm water is

$$V_0 = h_0 \pi \left(R_i^2 - a^2 \right). \tag{39}$$

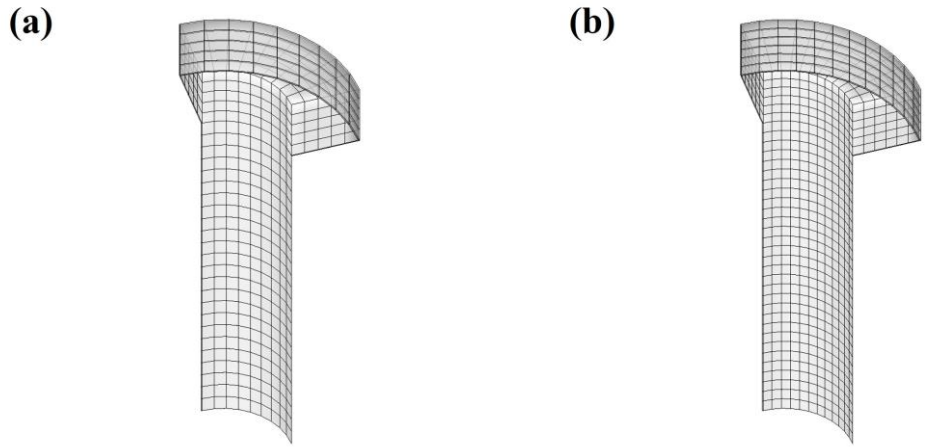

Fig. 4 Mesh discretization of the body surface and the inner free surface in a quarter area for d = 3 m, R_e = 6 m, e = 0.06 m, and h = 20 m with different discretization schemes: (a) Mesh 1, and (b) Mesh 2

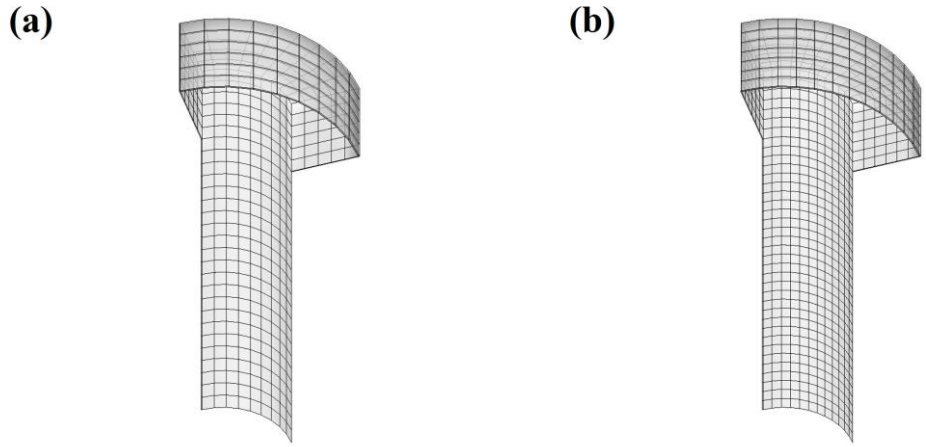

Fig. 5 Mesh discretization of the body surface and the inner free surface in a quarter area for d = 4 m, R_e = 6 m, e = 0.06 m, and h = 20 m with different discretization schemes: (a) Mesh 3, and (b) Mesh 4

To ensure the present results are reliable, the convergence of the present results with respect to the mesh discretization is examined. In the convergence test, an OWC device with its exterior radius R_e = 6 m is concerned. The thickness of the stiffening plates and that of the exterior shell is 0.06 m, i.e. e = 0.06 m. In the meantime, the draft of the

device is varied as d = 3 m and 4 m, respectively. The incident wave travels along the positive x-axis, and the incident wave amplitude A is 1 m. In the calculation, two geometric symmetry planes are adopted to facilitate the calculation. For d = 3 m, two discretization schemes, namely Mesh 1 and Mesh 2, are employed. In Mesh 1, 525 quadrilaterals elements are used in each quadrant (480 elements on the body surface, and 45 elements on the inner water plane area). In Mesh 2, 818 quadrilateral elements are used in each quadrant (746 elements on the body surface, and 72 elements on the inner water plane area). For d = 4 m, another two discretization schemes, namely Mesh 3 and Mesh 4, are employed. In Mesh 3, 542 quadrilaterals elements are used in each quadrant (497 elements on the body surface, and 45 elements on the inner water plane area). In Mesh 4, 861 quadrilateral elements are used in each quadrant (789 elements on the body surface, and 72 elements on the inner water plane area). The mesh discretizations based on different schemes are shown in Figs. 4 and 5. The variation of C_a, C_b, χ_{opt}, and q_D with respect to ω is shown in Fig. 6. Even though the mesh discretizations in Mesh 1 and Mesh 3 are much coarser than those in Mesh 2 and Mesh 4, the different discretizations lead to almost the same results, which indicates that the convergence is achieved.

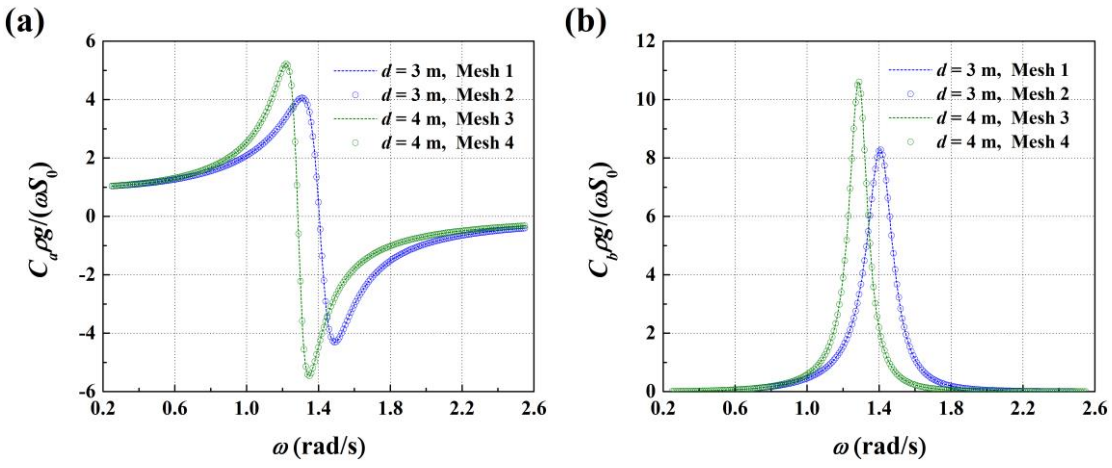

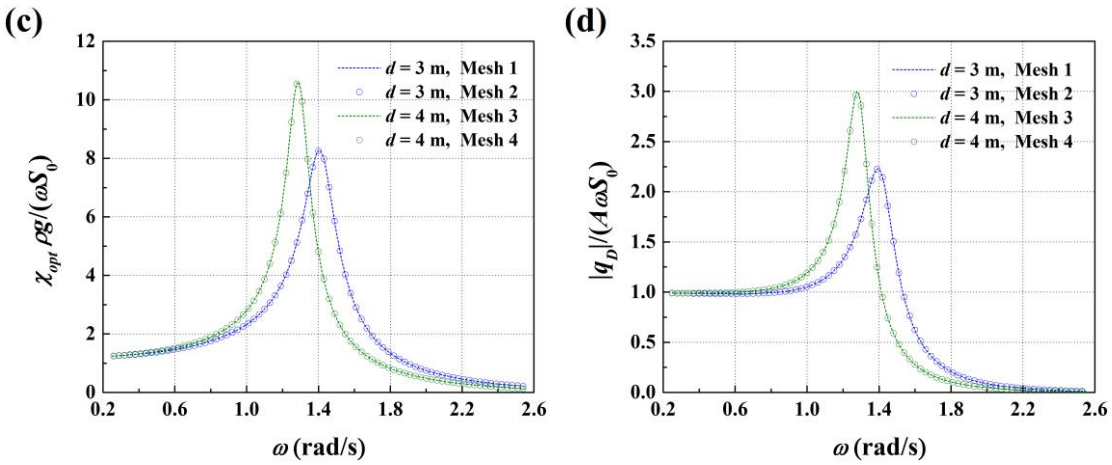

Fig. 6 Comparison of the calculation results of C_a, C_b, χ_{opt}, and q_D based on different mesh discretizations with R_e = 6 m, e = 0.06 m, h = 20 m, A = 1 m, and β = 0 for (a) C_a, (b) C_b, (c) χ_{opt}, and (d) q_D.

After obtaining C_a, C_b, and q_D, the total volume flux q_c and the oscillating air pressure p_c can be determined immediately based on Eq. (28). For the purpose of validation, an alternative solution of q_c and p_c has also been developed. The detailed deviation of this solution is introduced in the Appendix. In the alternative solution, q_c and p_c are related to the incident wave and the propagation modes of the radiation wave in the far field. The calculation of q_c and p_c is achieved without the solution of the diffraction problem. A comparison of q_c and p_c based on different methods is then made. In the calculations, the turbine parameter is equal to the optimal one, i.e. $\chi = \chi_{opt}$, and the comparison is shown in Fig. 7. In Fig. 7, 'Direct' refers to the results based on the method shown in Sections 2, 3, and 4, and 'Indirect' represents those based on the alternative method. In Fig. 7, an excellent agreement is achieved between the results based on different methods, validating the present solution.

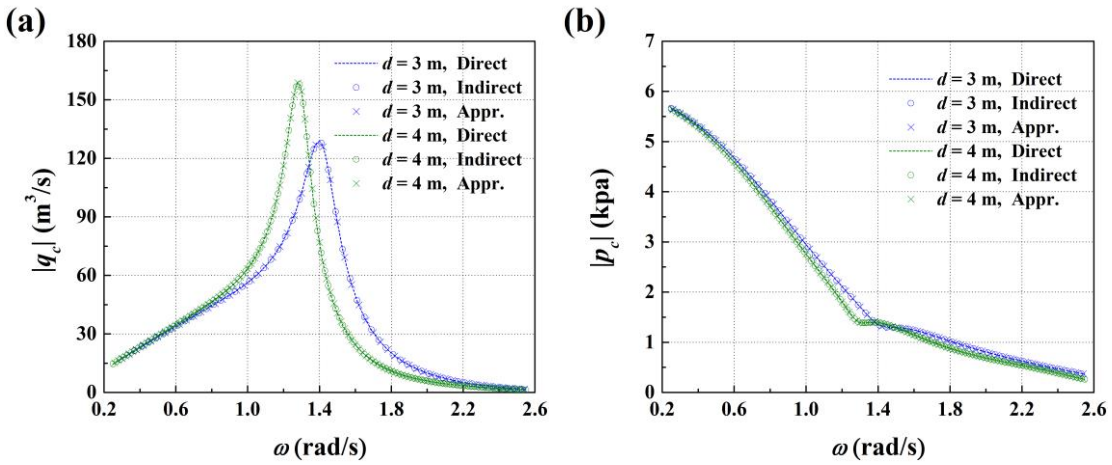

404

405 Fig. 7 Comparison of the calculation results of q_c and p_c based on different methods with R_e =
406 6 m, e = 0.06 m, h = 20 m, A = 1 m, β = 0, and $\chi = \chi_{opt}$ for (a) q_c, and (b) p_c.

407

408 To further examine the validity of the developed model, a comparison with the
409 reported data is then conducted. Martins-Rivas and Mei [19] studied the performance
410 of an OWC installed at the tip of a long breakwater. When the incident wave travels
411 along the thin breakwater, the effect of the breakwater can be neglected, and the case is
412 reduced to a truncated hollow column. An OWC in a shape of a truncated hollow
413 column has also been considered in Deng et al. [41]. We then consider a truncated
414 hollow column with an inner radius a_c, thickness $0.002a_c$, and draft $0.4a_c$. The water
415 depth h equals $2a_c$. In the numerical simulation, 340 elements are used in each quadrant
416 (195 elements on the body surface, and 145 elements on the inner water plane area).
417 The present results are compared with the analytical results in Martins-Rivas and Mei
418 [19] and Deng et al. [41]. Fig. 8 shows a good agreement between the results based on
419 different methods.

420

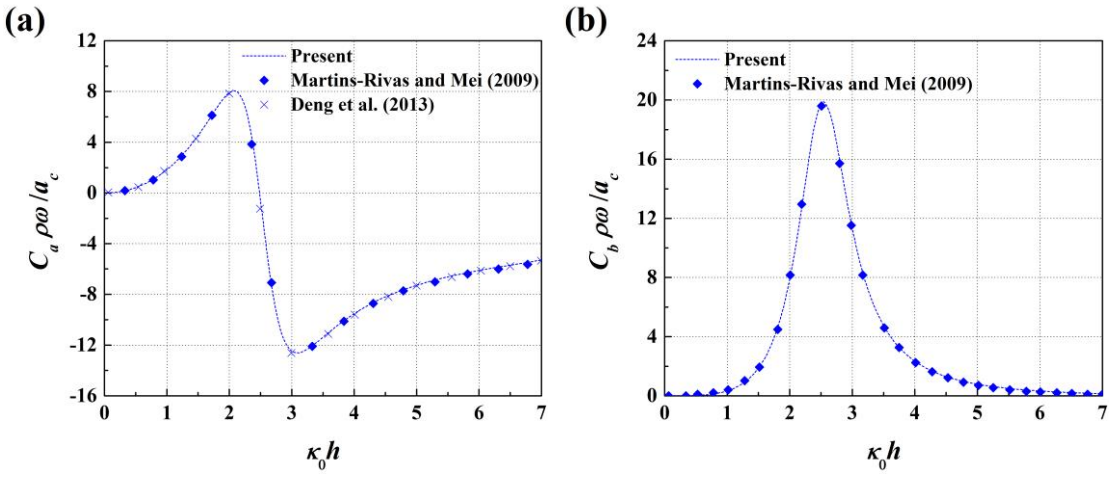

Fig. 8 Comparison of the calculation results for a truncated hollow column with analytical results for (a) C_a, and (b) C_b.

6. Numerical results and discussion

Detailed numeral studies are conducted in this section. All the results shown in this section are in full scale, and numerical results for regular and irregular sea conditions are both presented and discussed. In addition, in the subsequent calculations, the water depth is fixed at h = 20 m.

6.1 Regular sea states

The performance of the system in regular sea states is firstly examined. In the calculations, the incident wave amplitude is fixed at A = 1 m, and wave frequency varies from 0.25 rad/s to 2.55 rad/s. The variation of q_c, p_c, W_c, and E_c with respect to wave frequency is then illustrated.

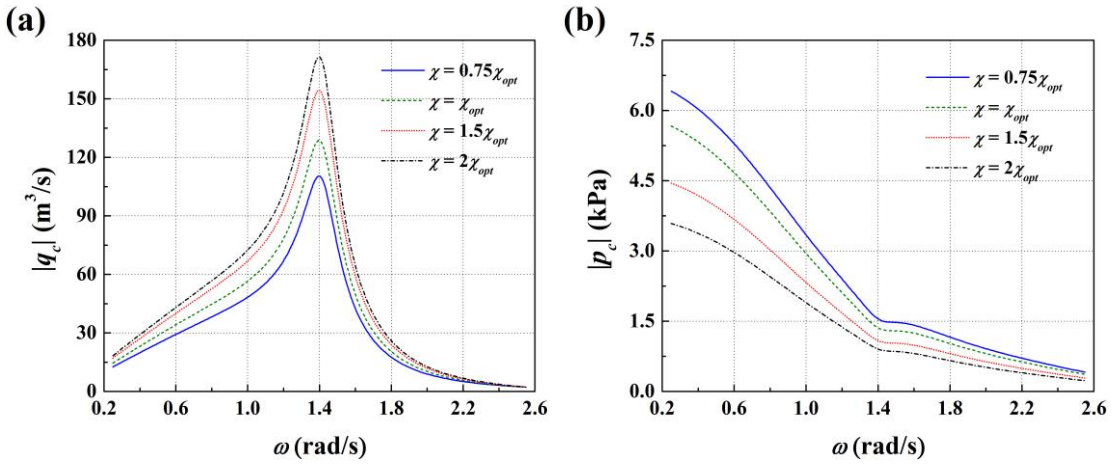

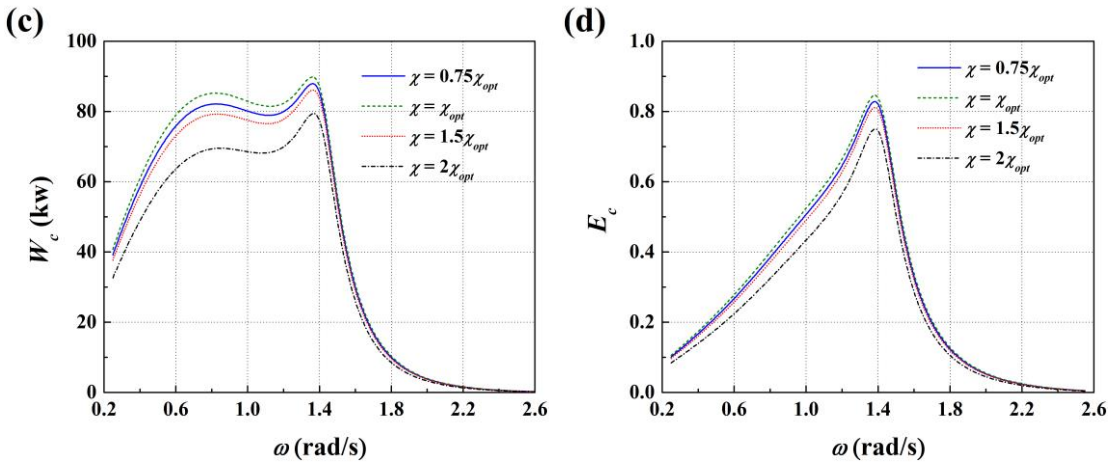

437

438 Fig. 9 Effect of the turbine parameter χ on q_c, p_c, W_c, and E_c with R_e = 6 m, d = 3 m, e =
439 0.06 m, h = 20 m, A = 1 m, and β = 0 for: (a) q_c, (b) p_c, (c) W_c, and (d) E_c
440

441 Effect of the turbine parameter χ on q_c, p_c, W_c, and E_c is shown in Fig. 9 with e =
442 0.06 m, d = 3 m, and R_e = 6 m. χ varies from 0.75 to 2 times the optimal turbine
443 parameter. In addition, the wave heading is fixed at β = 0. The turbine parameter χ can
444 be adjusted by some ways, such as varying the rotational speed N. An increase of the
445 rotational speed N can cause a decrease of χ (see Eq. (7a)). From Figs. 9(a) and 9(b),
446 we note that a decrease of the turbine parameter χ reinforces the damping effect imposed
447 on the inner free surface, and then leads to a decrease of the volume flux and an increase
448 of the oscillating air pressure. In Fig. 9(c), the maximum wave power absorption is
449 attained when $\chi = \chi_{opt}$ at a certain wave frequency. In Fig. 9(d), the wave energy
450 extraction efficiency firstly continues to increase with the increase of ω until it reaches
451 a prominent peak at ω = 1.38 rad/s. When ω exceeds 1.38 rad/s, it decays quickly until
452 vanished. A deviation of the turbine parameter from $\chi = \chi_{opt}$ causes a decrease of the
453 peak value and narrows down the frequency bandwidth in which high energy extraction
454 efficiency can be achieved. The effect of the air compressibility on W_c and E_c is then
455 examined. As shown in Fig. 10, the ignorance of the air compressibility (i.e. $\mu = 0$) leads
456 to an obvious overestimation of the W_c and E_c especially when the frequency is less than
457 the resonance frequency of the piston-mode motion.

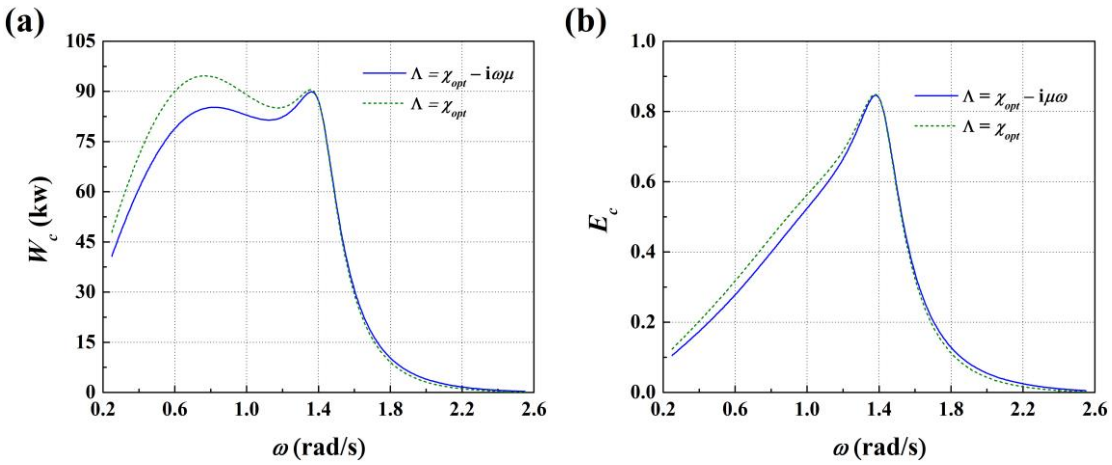

458

459 Fig. 10 Effect of the air compressibility on W_c, and E_c with R_e = 6 m, d = 3 m, e = 0.06 m, h =
460 20 m, A = 1 m, β = 0, and $\chi = \chi_{opt}$ for: (a) W_c, and (b) E_c.
461

462 The distribution of the wave elevation in the vicinity of the combined system at ω =
463 1.38 rad/s is calculated and shown in Fig. 11 with different turbine parameters. $\chi = +\infty$
464 corresponds to a condition that the inner free surface open to the air, and the air turbine
465 is removed (N = 0). Around ω = 1.38 rad/s, the total volume flux maximises (see Fig.
466 9(b)), and the captured wave power attains a local maximum (see Fig. 9(c)). In addition,
467 at this frequency, the radiation susceptance vanishes (see Fig. 6(a)), and the radiation
468 conductance maximises (see Fig. 6(b)). It suggests that this frequency corresponds to
469 the piston (or pumping) natural frequency of the water column in a moonpool. As a
470 result, when the inner free surface is open to the air, significantly amplified wave
471 elevation is observed at this wave frequency (see Fig. 11(a)). In Fig. 11(a), the
472 distribution of the wave elevation within the whole chamber is almost uniform, and the
473 fluid within the chamber moves like a rigid body. With a decrease of the turbine
474 parameter, more damping effect is applied on the inner free surface, and the wave
475 elevation gradually loses its uniform distribution. Its magnitude varies more and more
476 apparently along the circumferential direction, causing a breakdown of the piston-like
477 motion.

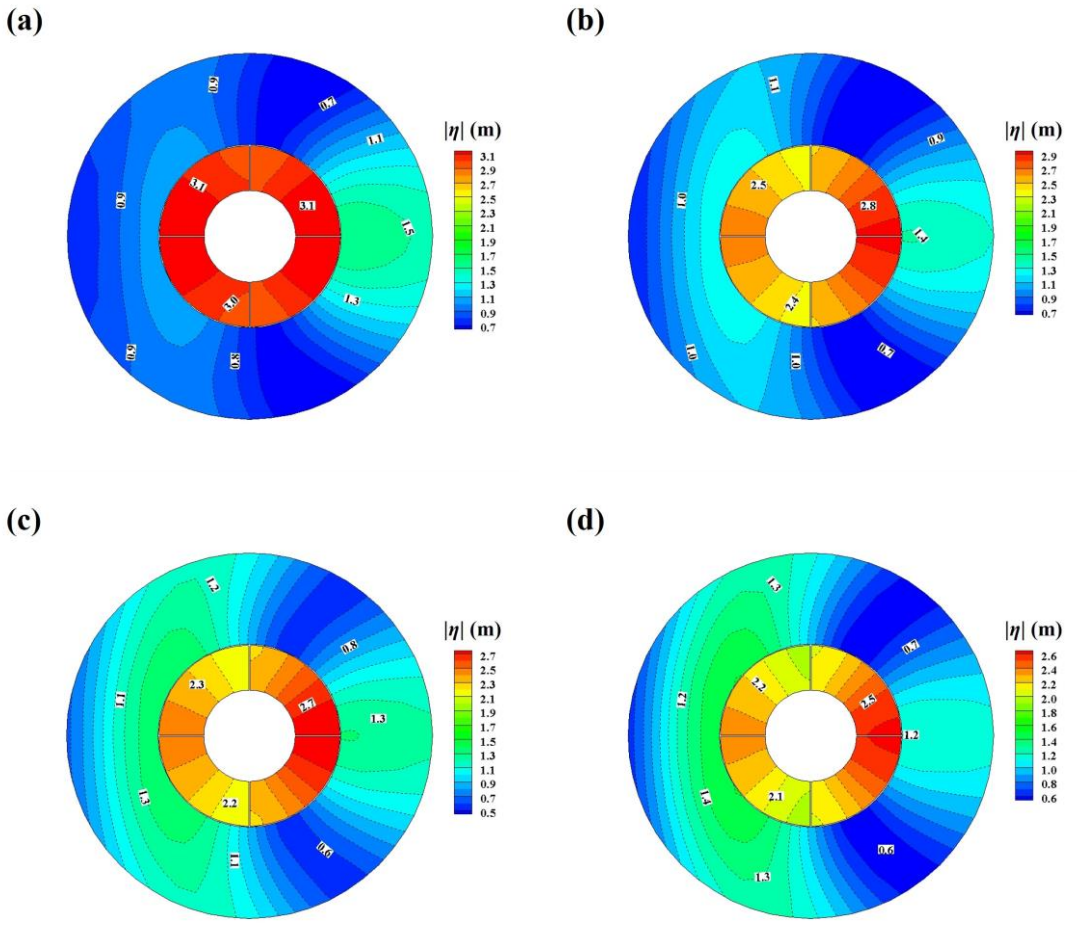

Fig. 11 Distribution of the surface elevation amplitude in the vicinity of the combined system at ω = 1.38 rad/s with R_e = 6 m, d = 3 m, e = 0.06 m, h = 20 m, A = 1 m, and β = 0 for (a) $\chi = +\infty$, (b) $\chi = 2\chi_{opt}$, (c) $\chi = \chi_{opt}$, and (d) $\chi = 0.5\chi_{opt}$

In the present study, vertical plates have been used to divide the whole chamber into four sub-chambers. Based on the assumption of thin plates, an approximate solution to q_c and p_c is developed in the Appendix, in which only the zeroth-order component of the incident wave is retained in the calculation. The results of q_c and p_c based on the approximate solution have been added into Fig. 7. As shown in Fig. 7, a good agreement is achieved between the approximate solution and the complete solution. It indicates that when the plates are thin, Eq. (A12) provides an effective way to evaluate q_c and p_c. Eq. (A12) shows that q_c and p_c are mainly contributed by the zeroth-order component of the incident wave, and the wave heading has almost no effect on q_c and p_c. As W_c and E_c can be evaluated directly from p_c and q_c, it suggests that

the wave heading also has a negligible effect on W_c and E_c.

We then examine the effect of the wave heading on the wave elevation in the vicinity of the system. The distribution of the wave elevation amplitude at ω = 1.38 rad/s is shown in Fig. 12 with β varying from 0 to π/4. Under different wave headings, the wave elevation within each sub-chamber distributes almost uniformly. As β increases, the wave elevation in the upstream and downstream sub-chambers gets enhanced, while in the remaining two sub-chambers, the wave elevation gets gradually less obvious. When β increases to π/4, the distribution of the wave elevation is symmetry with respect to θ = π/4, and significantly amplified wave elevation can be observed in the downstream sub-chamber.

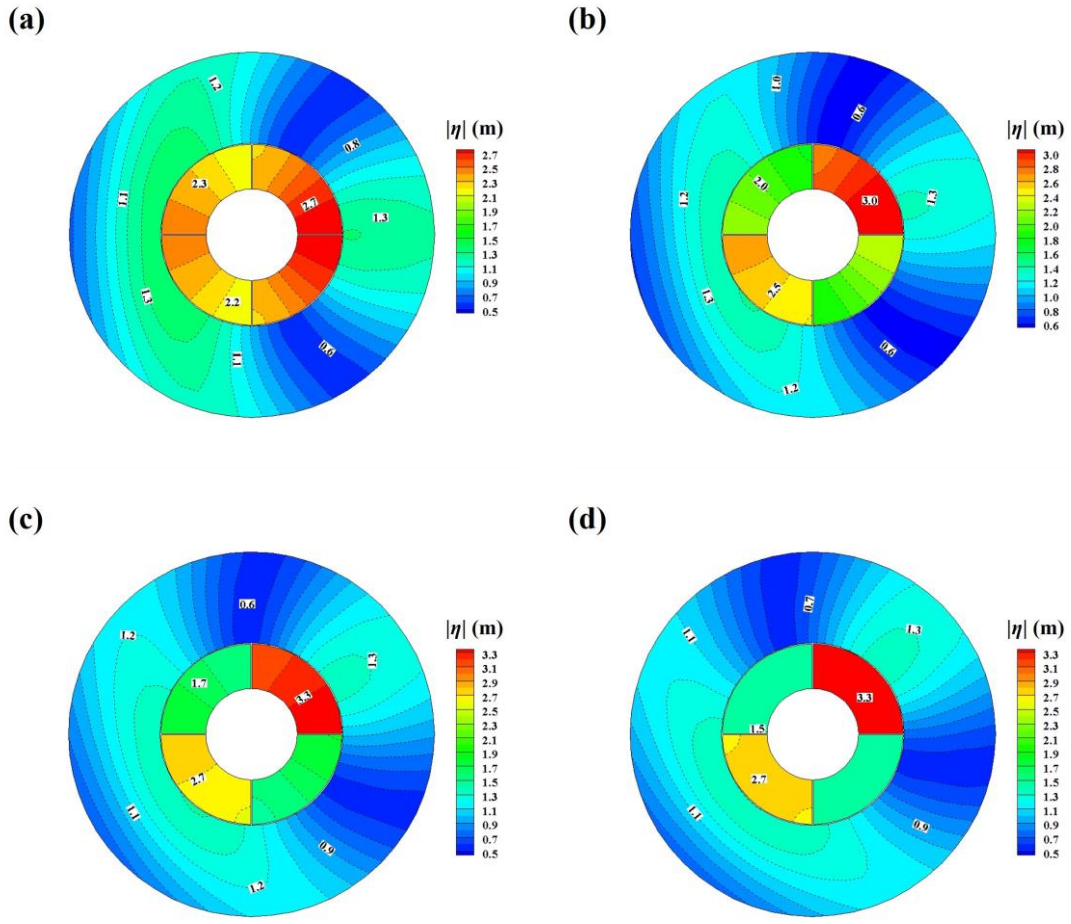

Fig. 12 Distribution of the surface elevation amplitude in the vicinity of the combined system at ω = 1.38 rad/s with R_e = 6 m, d = 3 m, e = 0.06 m, h = 20 m, A = 1 m, and $\chi = \chi_{opt}$ for (a) β = 0, (b) β = π/12, (c) β = π/6, and (d) β = π/4.

The effect of the plate thickness on q_c, p_c, W_c, and E_c is presented in Fig. 13 with $\chi = \chi_{opt}$. The thickness of the plates is varied as e = 0.03 m, 0.06 m, 0.09 m, and 0.12 m, respectively. From the indirect approach in the Appendix, we note that for a given incident wave, the wave power absorption by the OWC can be determined using the information of the radiation wave in the far field. In the pressure-dependent radiation problem, constant oscillating air pressure is applied on the inner free surface, and the fluid within the chamber moves almost uniformly like a rigid body. When the plates are thin, the effect of the plates on the piston-like fluid motion within the chamber as well as the radiation wave in the exterior region is negligible. Therefore, the presence of the thin plates makes a negligible impact on the performance of the OWC as shown in Fig. 13.

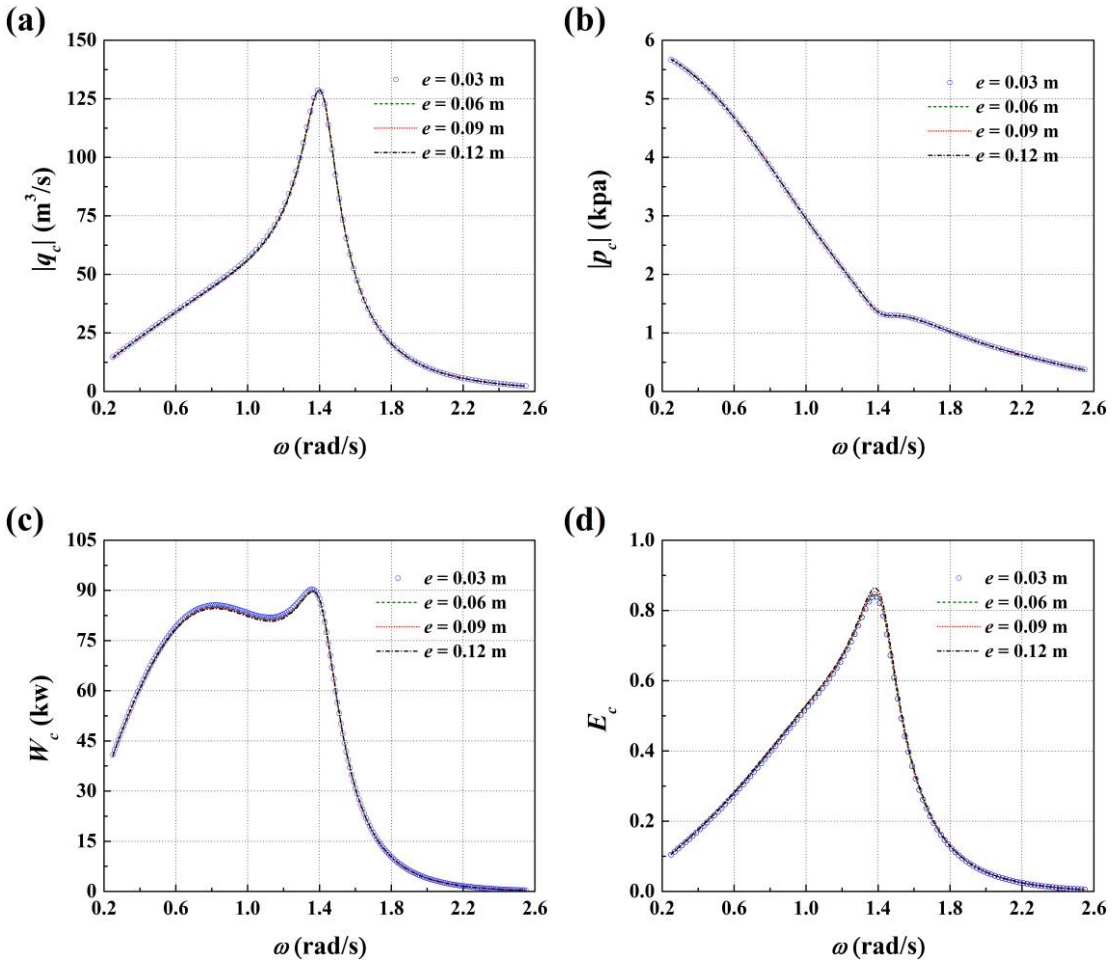

Fig. 13 Effect of the plate thickness on q_c, p_c, W_c, and E_c with R_e = 6 m, d = 3 m, h = 20 m, A = 1 m, β = 0, and $\chi = \chi_{opt}$ for (a) q_c, (b) p_c, (c) W_c, and (d) E_c

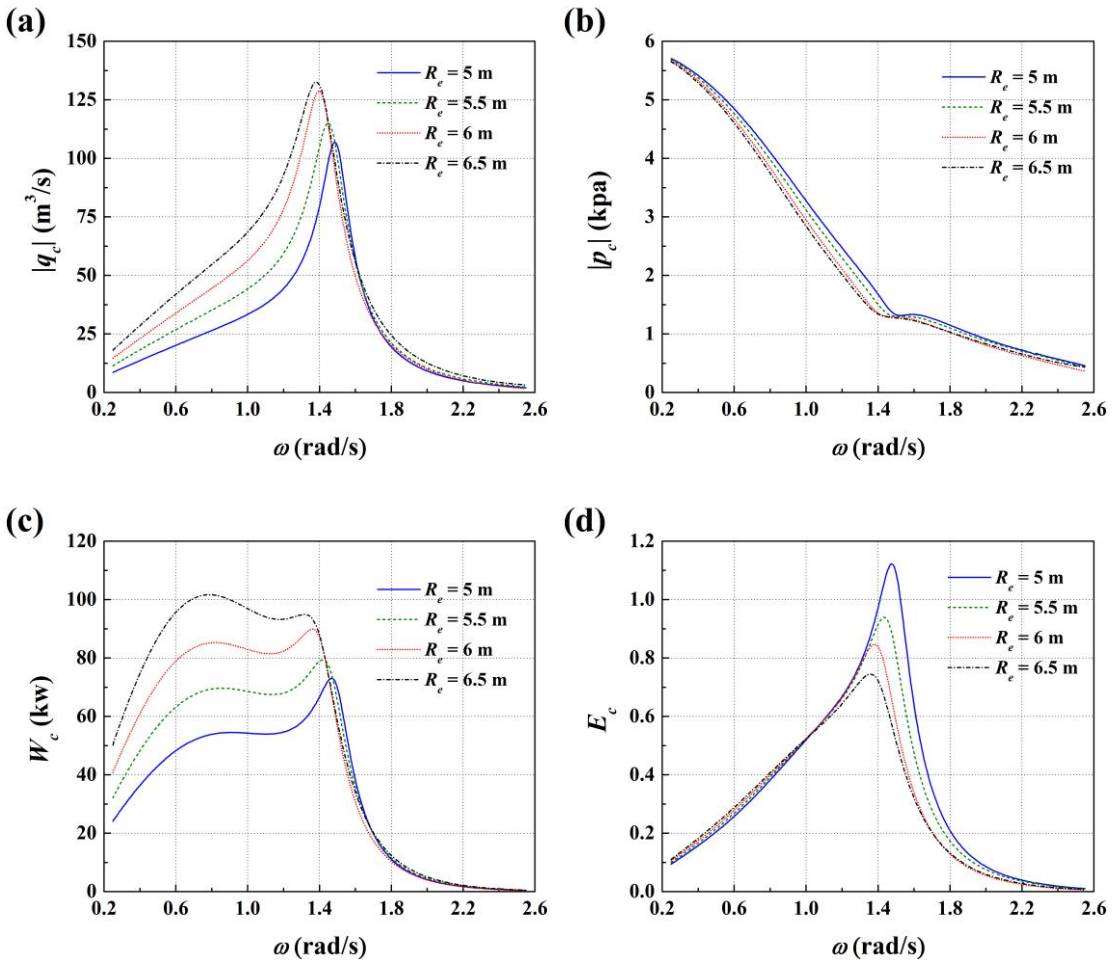

525

526

527 Fig. 14 Effect of the exterior radius of the chamber on q_c, p_c, W_c, and E_c with d = 3 m, e =

528 0.06 m, h = 20 m, A = 1 m, β = 0, and $\chi = \chi_{opt}$ for (a) q_c, (b) p_c, (c) W_c, and (d) E_c

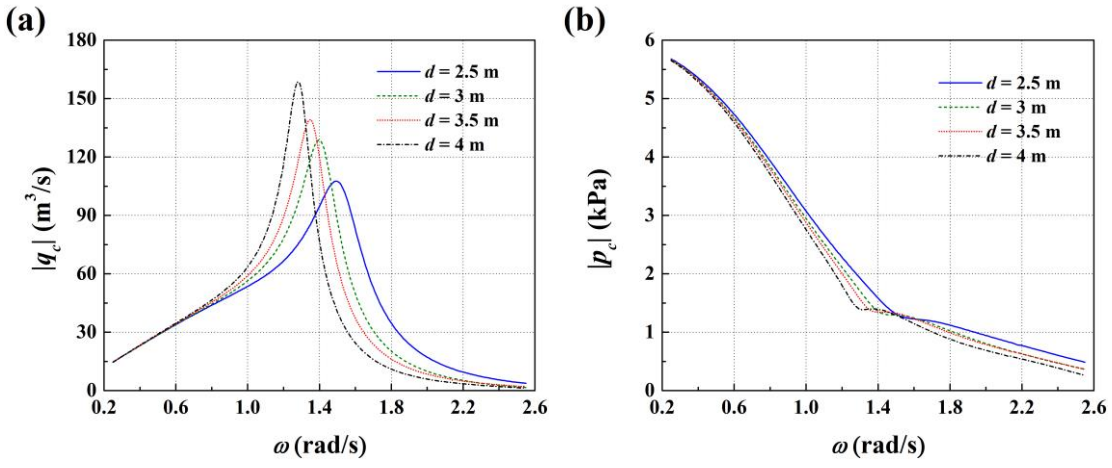

529

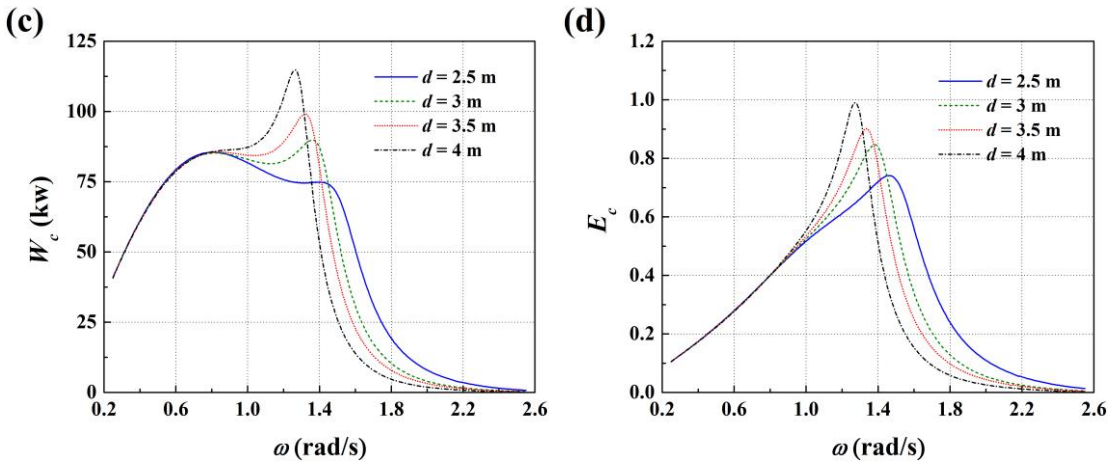

Fig. 15 Effect of the chamber draft on q_c, p_c, W_c, and E_c with R_e = 6 m, e = 0.06 m, h = 20 m, A = 1 m, β = 0 and $\chi = \chi_{opt}$ for (a) q_c, (b) p_c, (c) W_c, and (d) E_c

The effect of the exterior radius and draft of the air chamber on q_c, p_c, W_c, and E_c is presented in Figs. 14 and 15 with $\chi = \chi_{opt}$. The variation of the volume flux is characterized by a prominent peak (see Figs. 14(a) and 15(a)), at which significant piston-like fluid motion is induced in the chamber. An increase of the exterior radius or draft of the chamber can increase the amount of the entrapped fluid, and then moves the frequency of the apparent piston-like fluid motion to the low-frequency region. In Figs. 14(b) and 15(b), the air pressure continues to decrease with the increase of ω. In addition, at the frequency of the piston-like motion, obvious enhancements of W_c can be found (see Figs. 14(c) and 15(c)), and the maximum power extraction efficiency is attained (see Figs. 14(d) and 15(d)). In Figs. 14(d) and 15(d), a value of E_c over unity means that the capture width of the OWC exceeds $2(R_i - a)$. As remarked in Nader et al. [12], due to the diffraction of the incident wave around the OWC, the adequate wave power available to the device can be higher than that of the free incident wave passing the device. As a result, the value of E_c can be over unity. It is also noted that a decrease of the chamber width or an increase of the chamber depth can make the fluid entrapped inside the chamber perform more like a rigid body, enhancing the piston-like fluid motion. Then, reinforcement in the peak value of the energy extraction efficiency can be observed with a decrease of the chamber width or an increase of the chamber depth.

In addition, in real conditions, in order to maximise the device's efficiency, it is required to keep the wave power absorption by the device as high as possible in a broader band of wave conditions. Therefore, as shown in Fig. 15(c), it is preferable to have an OWC with a shallow draft which operates better at a larger wave frequency band, than a device with an increased draft.

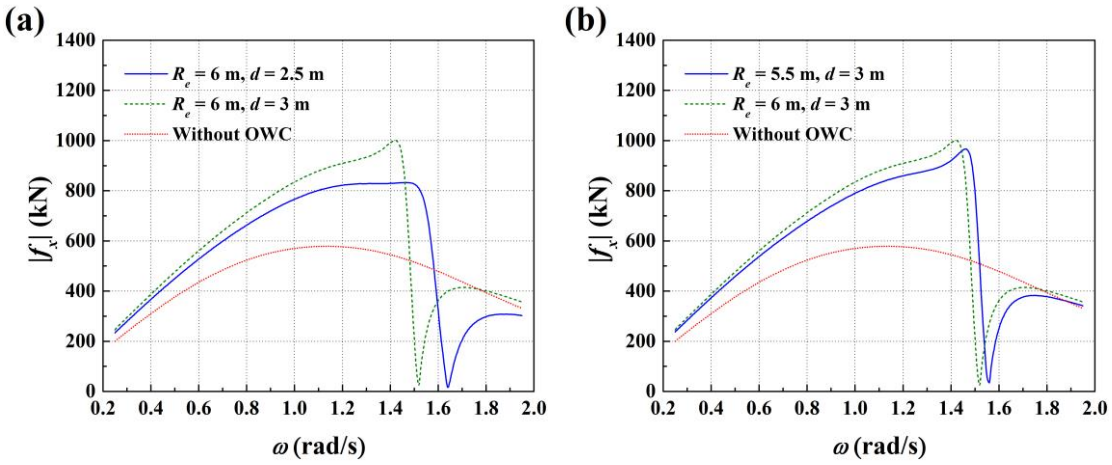

Fig. 16 Effect of the attached OWC on the wave force on the monopile: (a) R_e = 6 m, and (b) d = 3 m

The effect of the attached OWC on the wave force on the monopile is then examined. The wave forces on the systems with and without an attached OWC are compared. As shown in Fig. 16, for a wide range of wave frequencies, the presence of the OWC imposes additional wave force on the system. However, at specific wave conditions, the wave forces on the OWC and the monopile can balance each other, leading to a nearly zero net force on the whole system.

6.2 Irregular sea states

The hydrodynamic performance of the combined system in irregular sea states is then examined. The real sea conditions are always complex with irregular waves. Therefore, the Jonswap spectrum has been adopted in this study to describe the characteristics of the irregular waves. Following Goda [42], the spectra density function is expressed as

$$S(f) = \hat{\beta}_j H_S^2 T_p^{-4} f^{-5} \exp\left[-\frac{5}{4}(T_p f)^{-4}\right] \gamma^{\exp\left[-(T_p f - 1)^2 / (2\alpha^2)\right]}, \quad (41)$$

in which

$$\hat{\beta}_j = \frac{0.06238}{0.230 + 0.0336\gamma - 0.185\left(1.9 + \gamma\right)^{-1}}\left(1.094 - 0.01915\ln\gamma\right); \tag{42a}$$

$$\alpha = \begin{cases} 0.07, & f \le f_p, \\ 0.09, & f > f_p. \end{cases} \tag{42b}$$

In Eqs. (41), (42a) and (42b), T_p is the peak wave period; H_s is the significant wave height; $f = \omega/(2\pi)$; $f_p = 1/T_p$; γ is the peak enhancement factor, which takes a value of 3.3 in this study. The significant wave period T_s can be determined according to

$$T_s = \left[1 - 0.132\left(0.2 + \gamma\right)^{-0.559}\right]T_p. \tag{43}$$

In the following calculations, the exterior radius and draft of the chamber are fixed at R_e = 6 m and d = 3 m, respectively. The thickness of the stiffening plates and that of the exterior shell of the chamber are fixed at 0.02 times the radius of the monopile, i.e. $e = 0.02a$ = 0.06 m. In addition, in total, 7 test cases are used for irregular sea states. The test matrix for irregular sea states is listed in Table 1.

Table 1. Test matrix for irregular sea states

Case No.	H_s (m)	T_p (s)	T_s (s)	χ (m^3/s/Pa)	μ (m^3/Pa)	Spectrum
1	1.5	10	9.34	8.64×10^{-3}	1.66×10^{-3}	Jonswap
2	2	10	9.34	8.64×10^{-3}	1.66×10^{-3}	Jonswap
3	2.5	10	9.34	8.64×10^{-3}	1.66×10^{-3}	Jonswap
4	3	10	9.34	8.64×10^{-3}	1.66×10^{-3}	Jonswap
5	2	8	7.48	1.28×10^{-2}	1.66×10^{-3}	Jonswap
6	2	11	10.28	7.46×10^{-3}	1.66×10^{-3}	Jonswap
7	2	12	11.21	6.62×10^{-3}	1.66×10^{-3}	Jonswap

In the numerical implementation, a discretization of the wave spectrum is made. The wave spectrum is divided into M parts, and the frequency bandwidth dω in each part keeps the same and is defined by

$$\mathrm{d}\omega = \frac{\omega_H - \omega_L}{M}, \tag{44}$$

in which ω_H and ω_L are high and low cut-off frequencies, respectively. Then, the incident wave elevation can be expressed as a superposition of a series of the individual regular incident wave. That is

$$\Xi_I(t)=\sum_{j=1}^{M}A_j\cos\left[\kappa_j\left(x\cos\beta+y\sin\beta\right)-\omega_j t+\varepsilon_j\right]=\mathrm{Re}\left\{\sum_{j=1}^{M}A_j e^{i\left[\kappa_j\left(x\cos\beta+y\sin\beta\right)-\omega_j t+\varepsilon_j\right]}\right\}, \quad (45)$$

in which

$$\omega_j=\omega_L+\left(j-1+\tau_j\right)d\omega; \quad (46a)$$

$$A_j=\sqrt{2S\left(f_j\right)d\omega}. \quad (46b)$$

In Eqs. (45), (46a) and (46b), A_j, ω_j, and κ_j represent the amplitude, wave frequency, and wavenumber of the jth incident wave component, respectively; $f_j=\omega_j/(2\pi)$; ε_j is a random phase angle uniformly distributed in the range of [0, 2π]; τ_j is a random number uniformly distributed in [0,1]. τ_j is introduced to impart a random component to ω_j. Then, the phase-locking of the incident wave can be avoided. In this study, M = 240, ω_L = 0.25 rad/s, and ω_H = 2.65 rad/s are used. These parameters has been proved to be sufficient to represent the wave energy distribution of the target spectrum.

Similar to the incident wave, we can express the volume flux and the oscillating air pressure as a superposition of a serious of individual components. That is

$$Q_c(t)=\mathrm{Re}\left\{\sum_{j=1}^{M}q_{c,j}e^{-i\omega_j t}\right\}; \quad (47a)$$

$$P_c(t)=\mathrm{Re}\left\{\sum_{j=1}^{M}p_{c,j}e^{-i\omega_j t}\right\}. \quad (47b)$$

For the simulation concerning a given irregular sea state, we keep the turbine parameter χ and the chamber parameter μ both constant values, and do not vary with time. Then, after insetting Eq. (47a) and (47b) into Eq. (3), we can have

$$q_{c,j}=\Lambda_j p_{c,j}=\frac{\Lambda_j e^{i\varepsilon_j}q_{D,j}}{\Lambda_j-\left(-C_{b,j}+iC_{a,j}\right)}, \quad (48)$$

with

$$\Lambda_j = \chi - i\omega_j \mu, \tag{49}$$

in which $q_{D,j}$ is the complex amplitude of the volume flux in a wave diffraction problem by a regular incident wave with its frequency and amplitude being ω_j and A_j; $C_{a,j}$ and $C_{b,j}$ are the radiation susceptance and radiation conductance at a frequency of ω_j. The calculation of $q_{D,j}$, $C_{a,j}$ and $C_{b,j}$ can be achieved by using the numerical model developed in Sections 2, 3 and 4.

Besides the volume flux and the oscillating air pressure, the wave power absorption by the system can also be evaluated for irregular sea states. After inserting Eqs. (47a), (47b), and (48) into Eq. (13), we can obtain the following expression for the wave power absorption by the system in irregular sea states

$$W_c = \sum_{j=1}^{M} \left[\frac{1}{2} \chi \frac{\left| q_{D,j} \right|^2}{\left(\chi + C_{b,j} \right)^2 + \left(\omega_j \mu + C_{a,j} \right)^2} \right]. \tag{50}$$

To illustrate the effect of the turbine parameter on the wave power absorption, the variation of W_c with respect to χ is shown in Fig. 17 for Case 2, Case 5, Case 6, and, Case 7, respectively. It is found that in a specific irregular sea state, the maximum wave energy absorption can be achieved when χ is around $\chi_{opt\_T_s}$, in which $\chi_{opt\_T_s}$ represents the optimal turbine parameter for a regular incident wave with its period equal to T_s. $\chi_{opt\_T_s}$ can be evaluated using the numerical model established in Sections 2, 3 and 4, and $\chi = \chi_{opt\_T_s}$ is adopted for the irregular sea states. The choices of χ and μ are for different irregular sea states are listed in Table 1.

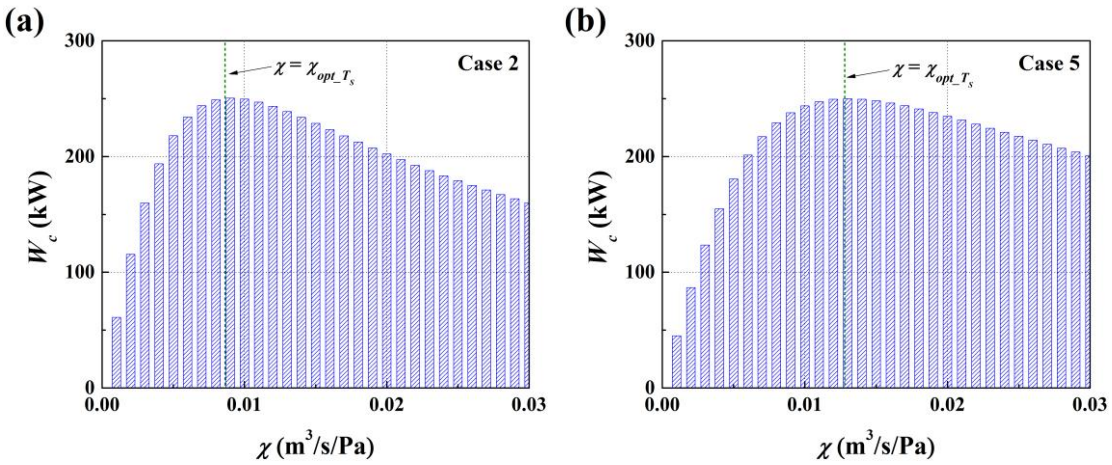

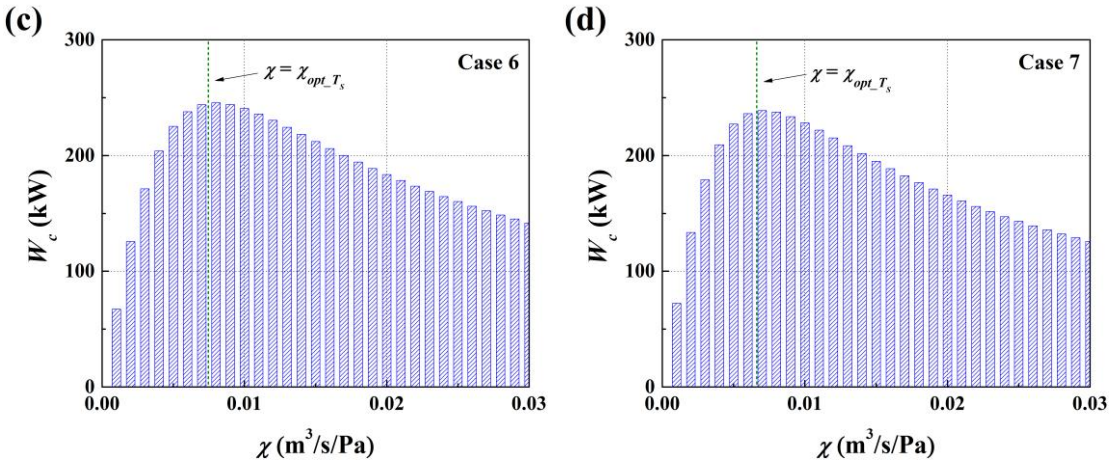

637

638 Fig. 17 Variation of the wave power absorption with respect to the turbine parameter for: (a) Case
639 2, (b) Case 5, (c) Case 6, and (b) Case 7
640

641 Figs. 18 shows the time history of the volume flux for Case 2, and Case 4 as an
642 example. As P_c follows a similar trend as Q_c, and hence is not shown for briefly. From
643 the time history, statistical information, such as the standard deviation, can be
644 determined. Hereinafter, we use σ_Q and σ_P to denote the standard deviation of the
645 volume flux and the oscillating air pressure, respectively.

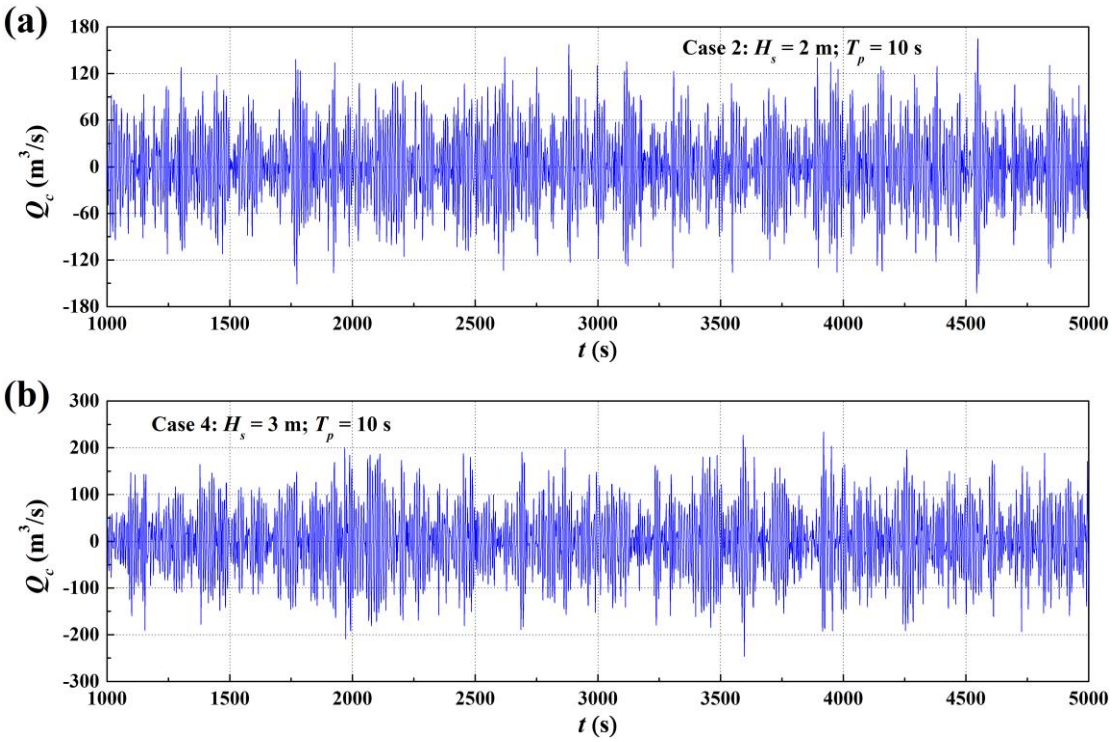

646

647

648 Fig. 18 Time history of the volume flux for (a) Case 2, and (b) Case 4

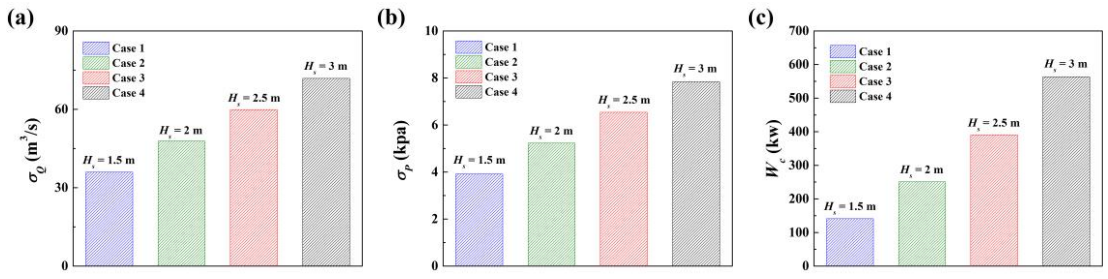

Fig. 19 Effect of the significant wave height on (a) σ_Q, (b) σ_P, and (c) W_c

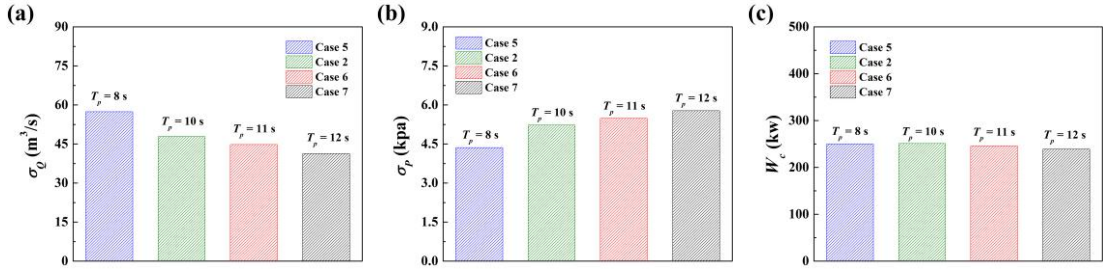

Fig. 20 Effect of the peak wave period on (a) σ_Q, (b) σ_P, and (c) W_c

The effect of the significant wave height is then examined. Fig. 19 shows a comparison of σ_Q, σ_P and W_c between Case 1, Case 2, Case 3, and Case 4 in the test matrix. Ren et al. [43] experimentally studied the performance of an oscillating buoy type wave energy converter integrated into a NREL 5 MW wind turbine. They suggested that to ensure the attached wave energy converter can function properly, H_s should be less than 6 m, and H_s = 6 m was used as a threshold for the operational sea states in their work. Following Ren et al. [43], a series of significant wave heights, which are all less than 6 m, i.e. H_s = 1.5 m, 2 m, 2.5 m and 3 m, have been adopted. As shown in Fig. 19, σ_Q and σ_P both continue to increase with the increase of H_s. When H_s is 2 m, W_c can reach 251 kW. As H_s increases further, W_c grows in an almost quadratic manner, and a larger amount of wave power can be absorbed. However, it should also be noted that due to the losses of the air turbine as well as those of the electric generator, the actual wave power absorption can be less than the predicted value. It indicates that even when the size of the attached OWC is not large, i.e. R_e = 6 m and d = 3 m, by adopting an optimal turbine parameter, the wave power captured by the OWC can be an important supplement to the wind power production.

We then examine the effect of the peak wave period. Fig. 20 shows a comparison of

671 σ_Q, σ_P and W_c between Case 2, Case 5, Case 6 and Case 7 in the test matrix. It is
672 found that σ_Q decreases gradually as the peak wave period increases from 8 s to 12 s,
673 and σ_P exhibits a reversed trend. This is similar to the observation in regular sea states
674 (see Figs. 9(a, b). As shown in Fig. 9(c), T_p = 8 s, 10 s, 11 s and 12 s are all in the
675 frequency range of obvious wave power absorption. Therefore, with T_p = 8 s, 10 s, 11
676 s and 12 s, obvious wave power can be absorbed by the system in irregular sea states.
677
678 **7. Conclusions**
679 The wave interaction with a combined system consisting of an OWC and an offshore
680 wind turbine supported by a monopile foundation is investigated. The attached OWC
681 is of annular cross-section and consists of four fan-shaped sub-chambers. Numerical
682 models based on HOBEM are developed to evaluate the performance of the combined
683 system. A detailed numerical analysis is conducted for the case of an OWC integrated
684 into a NREL 5 MW wind turbine. The main conclusions of this study are summarized
685 as follows:
686 1) To examine the validity of the proposed model, two approaches, namely 'Direct'
687 and 'Indirect', are developed in this study. A comparison of the volume flux and
688 oscillating air pressure based on the two approaches is made, and a favorable agreement
689 is achieved. In addition, the present numerical results also agree well with the published
690 analytical results for OWCs of fundamental geometry.
691 2) Within the chamber, four stiffening plates are used to connect the exterior shell of
692 the OWC and the monopile foundation. When the plates are thin in thickness, they have
693 almost no effect on the wave power absorption. The maximum wave energy extraction
694 efficiency is attained when the significant piston-like fluid motion is induced within
695 each sub-chamber. When the incident wave travels along a direction where a stiffening
696 plate is installed, the piston-like motions in different sub-chambers are with almost the
697 same amplitude. As the incident wave deviates gradually form this direction, the piston-
698 like motions in the upstream and downstream sub-chambers get enhanced. In contrast,
699 those in the remaining sub-chambers gets less apparent.
700 3) The air compressibility makes a negative effect on the wave power absorption of

701 the OWC especially when the wave frequency is less than the resonance frequency of
702 the piston-mode motion of the fluid in the chamber. When attaching an OWC into a
703 monopile foundation, the wave forces on the OWC and the monopile can balance each
704 other at specific wave conditions, leading to a nearly zero net force on the whole system.
705 4) The resonance frequency of the piston-mode motion depends on the geometry of
706 the OWC. The resonance frequency can be adjusted to match the incident waves by
707 varying the size of the OWC, such as the draft and exterior radius. An increase in the
708 width or draft of the chamber can move the resonance frequency to the low-frequency
709 region. In addition, a decrease of the chamber width or an increase of the chamber depth
710 makes the fluid entrapped inside the chamber perform more like a rigid body. Then, the
711 piston-like fluid motion can be excited more evidently, and the corresponding energy
712 extraction efficiency is obviously enhanced.
713 5) Besides the geometric parameters, the turbine parameter is also an essential factor
714 affecting the wave power adsorption. An increase of the rotational speed of the air
715 turbine can reinforce the damping effect applied on the inner free surface, causing a
716 decrease of the volume flux and an increase of the oscillating air pressure. With an
717 optimal turbine parameter, significant energy extraction efficiency can be achieved. A
718 deviation from the optimal parameter can lead to a decrease of the wave power
719 absorption, and narrow down the frequency bandwidth of the obvious energy extraction
720 efficiency.
721 6) An approximation approach to the volume flux and the oscillating air pressure is
722 developed, in which a Fourier expansion of the velocity potential with respect to θ is
723 made, and only the zeroth-order component is retained in the calculation. A comparison
724 between the approximate and complete solutions is made, and the comparison shows
725 that when the plates are thin, the volume flux and the oscillating air pressure within the
726 chamber is mainly contributed by the zeroth-order component of the incident waves. It
727 also shows that the wave power absorption by the proposed system is not restricted by
728 the wave direction.
729 7) The performance of the attached OWC in irregular sea conditions is assessed. In

an irregular sea condition, the maximum wave energy absorption can be achieved when the turbine parameter is around the optimal one at the significant wave period. By adopting an optimal turbine parameter, the captured wave power can exceed 250 kW even when the size of the OWC is not large (i.e. R_e = 6 m, and d = 3 m) and in an operational sea condition (i.e. H_s = 2 m, and T_p = 10 s). As wave height increases further, a larger amount of wave power absorption can be expected. It indicates that the wave power absorption by the OWC can be an important supplement to the combined system, and the proposed combined system is a promising option for the further development.

In this study, we assume that the relative changes in the density and volume of the air in the chamber are small, and a linear air turbine is considered and a linear wave theory is adopted. The characteristic nature of a hydrodynamic or thermodynamics problem can be better described by a nonlinear analysis. The investigation of the effect of the nonlinearity arising from the incident wave and the air turbine can be of great importance, and this provides an interesting research topic for further study.

Acknowledgments

The work is financially supported by the National Natural Science Foundation of China (Grant Nos. 51809037, 51879039).

Appendix: An alternative solution to the volume flux and air pressure

An alternative solution to the volume flux, air pressure, and wave power captured by the OWC device is introduced in the Appendix. Besides the method introduced in Sections 2, 3, and 4, it is also possible to derive a solution of q_D based on the following manner. As $\hat{\phi}$ and ϕ_R both satisfy the Laplace's equation, the application of Green's second identity to $\hat{\phi}$ and ϕ_R in the whole fluid domain leads to

$$\iint_{S_b+S_e+S_i+S_d+S_\infty} \left(\phi_R \frac{\partial \hat{\phi}}{\partial n} - \hat{\phi} \frac{\partial \phi_R}{\partial n} \right) ds = 0, \tag{A1}$$

in which S_∞ is a cylindrical control surface surrounding the body, and its radius tends to infinity. By making use of the boundary conditions in Eqs. (20), (21) and (22), and

owning to the fact that ϕ_D and ϕ_R both satisfy a Sommerfeld condition in the far-field region, Eq. (A1) can be rewritten in the following form

$$\iint_{S_i} \hat{\phi} ds = -\iint_{S_\infty} \left(\phi_R \frac{\partial \phi_I}{\partial r} - \phi_I \frac{\partial \phi_R}{\partial r} \right) ds. \tag{A2}$$

Then, we can have

$$q_D = \iint_{S_i} \frac{\partial \hat{\phi}}{\partial z} ds = -\frac{\omega^2}{g} \iint_{S_\infty} \left(\phi_R \frac{\partial \phi_I}{\partial r} - \phi_I \frac{\partial \phi_R}{\partial r} \right) ds. \tag{A3}$$

In the exterior region ($r \geq R_e$), we can expand the incident and radiation potentials into a Fourier series with respect to θ

$$\phi_I = \sum_{m=-\infty}^{+\infty} A_m J_m(\kappa_0 r) Z_0(\kappa_0 z) e^{im\theta}; \tag{A4a}$$

$$\phi_R = \sum_{m=-\infty}^{+\infty} \left[B_{m0} H_m(\kappa_0 r) Z_0(\kappa_0 z) + \sum_{j=1}^{\infty} B_{mj} K_m(\kappa_j r) Z_j(\kappa_j z) \right] e^{im\theta}, \tag{A4b}$$

in which κ_j ($j \geq 1$) is the jth positive real root of $-\omega^2 = g\kappa_j \tan(\kappa_j h)$; $J_m(\cdot)$ is the Bessel function of order m; $H_m(\cdot)$ is the Hankel function of the first kind of order m; $K_m(\cdot)$ is the modified Bessel function of the second kind of order m; $Z_j(\kappa_j z)$ is an orthonormal function given at the interval $[-h, 0]$. The expression of $Z_j(\kappa_j z)$ is given by

$$Z_j(\kappa_j z) = \begin{cases} \dfrac{\cosh \kappa_0 (z+h)}{\cosh \kappa_0 h}, & j = 0, \\ \dfrac{\cos \kappa_j (z+h)}{\cos \kappa_j h}, & j \geq 1. \end{cases} \tag{A5}$$

The coefficients A_m and B_{mj} ($j \geq 0$) in Eq. (A4b) can be determined according to the following expression

$$A_m = -\frac{iAg}{\omega} i^m e^{-im\beta}, \tag{A6}$$

and

$$B_{m0} = -\frac{i}{4} \frac{1}{N_0(\kappa_0 h)} \iint_{S_b + S_i} \left(\phi_R \frac{\partial}{\partial n} - \frac{\partial \phi_R}{\partial n} \right) \left[J_m(\kappa_0 r) Z_0(\kappa_0 z) e^{-im\theta} \right] ds; \tag{A7a}$$

$$B_{mj} = -\frac{1}{2\pi}\frac{1}{N_j(\kappa_j h)}\iint_{S_b+S_i}\left(\phi_R\frac{\partial}{\partial n}-\frac{\partial\phi_R}{\partial n}\right)\left[I_m(\kappa_j r)Z_j(\kappa_j z)e^{-im\theta}\right]ds, \quad j\geq 1, \quad \text{(A7b)}$$

in which $I_m(\cdot)$ is the modified Bessel function of the first kind of order m; $N_j(\kappa_j h)$ represents the inner products of the vertical eigenfunction $Z_j(\kappa_j z)$ in [–h, 0], and is defined by

$$N_j(\kappa_j h) = \int_{-d}^{0} Z_j^2(\kappa_j z)dz = \begin{cases} \dfrac{1}{\cosh^2\kappa_0 h}\dfrac{h}{2}\left(1+\dfrac{\sinh 2\kappa_0 h}{2\kappa_0 h}\right), & j=0, \\ \dfrac{1}{\cos^2\kappa_j h}\dfrac{h}{2}\left(1+\dfrac{\sin 2\kappa_j h}{2\kappa_j h}\right), & j\geq 1. \end{cases} \quad \text{(A8)}$$

In the indirect approach, the body surface and inner free surface is discretized into a set of elements. The radiation potentials ϕ_R on S_b and S_i are obtained by solving Eq. (26), and the integration in Eq. (A7) is performed numerically by means of a Gaussian quadrature formula.

In the far-field region, the contribution from the evanescent modes to ϕ_R can be neglected owning to the fact that $K_m(\kappa_j r)$ attenuates exponentially with distance. Then, after inserting Eq. (A4) into Eq. (A3) and using Wronskian relationships for Bessel functions, the following expression for q_D can be obtained

$$q_D = \frac{\omega^2}{g}\sum_{m=-\infty}^{+\infty} 4iA_m B_{-m0}(-1)^m N_0(\kappa_0 h). \quad \text{(A9)}$$

With the solution of q_D, the total volume flux and the oscillating air pressure can be evaluated based on Eq. (28). Then, we can have

$$q_c = \frac{4i\rho\Lambda\omega^2}{\rho g\Lambda + i\omega q_R}\sum_{m=-\infty}^{+\infty} A_m B_{-m0}(-1)^m N_0(\kappa_0 h); \quad \text{(A10a)}$$

$$p_c = \frac{4i\rho\omega^2}{\rho g\Lambda + i\omega q_R}\sum_{m=-\infty}^{+\infty} A_m B_{-m0}(-1)^m N_0(\kappa_0 h). \quad \text{(A10b)}$$

In Eq. (A10), the total volume flux and the oscillating air pressure within the chamber is related to the incident wave as well as the radiation wave, while not depends on the diffraction wave. Eq. (A10) provides an alternative way for the evaluation of q_c and p_c.

Table A1. Variation of the magnitude of q_D (in m^3/s) with respect to M with $R_e = 6$ m, $e = 0.06$ m, $d = 3$ m and $h = 20$ m

M = \ ω =	0.3 rad/s	0.6 rad/s	0.9 rad/s	1.2 rad/s	1.5 rad/s
0	0.245×10^2	0.487×10^2	0.752×10^2	0.131×10^3	0.160×10^3
2	0.245×10^2	0.487×10^2	0.752×10^2	0.131×10^3	0.160×10^3
5	0.245×10^2	0.487×10^2	0.752×10^2	0.131×10^3	0.160×10^3
10	0.245×10^2	0.487×10^2	0.752×10^2	0.131×10^3	0.160×10^3

Table A2. Variation of the magnitude of q_D (in m^3/s) with respect to M with $R_e = 6$ m, $e = 0.06$ m, $d = 4$ m and $h = 20$ m

M = \ ω =	0.3 rad/s	0.6 rad/s	0.9 rad/s	1.2 rad/s	1.5 rad/s
0	0.245×10^2	0.494×10^2	0.806×10^2	0.207×10^3	0.636×10^2
2	0.245×10^2	0.494×10^2	0.806×10^2	0.207×10^3	0.636×10^2
5	0.245×10^2	0.494×10^2	0.806×10^2	0.207×10^3	0.636×10^2
10	0.245×10^2	0.494×10^2	0.806×10^2	0.207×10^3	0.636×10^2

When Eq. (A9) is adopted to calculate q_D, in total $2M + 1$ Fourier modes (from mode $(-M)$ to mode M) are used in the numerical implementation. The variation of q_D with respect to M is shown in Table A1 with $R_e = 6$ m, $e = c = 0.06$ m, $d = 3$ m, and $h = 20$ m. Analogous results to those in Table A1 but with $d = 4$ m is shown in Table A2. From Tables A1 and A2, it can be seen that the results exhibit almost no variation with respect to M. Other than the zeroth-order Fourier component, other components make almost no contribution to q_D. In the pressure-dependent radiation problem, the air pressure distributes nearly uniformly within the chamber, and the fluid within the chamber moves like a rigid body. As the plates are very thin, their effect on the fluid motion within the chamber is not obvious. In the exterior region, the radiation wave has almost no variation in the circumferential direction. Therefore, in Tables A1 and A2, the results of q_D are dominated by the zeroth-order component. Then, q_D can be efficiently calculated based on

$$q_D \approx 4A\omega B_{00} N_0(\kappa_0 h). \tag{A11}$$

Based on Eq. (A11), we can obtain the following expressions for the approximate evaluation of the q_c and p_c, which are given by

$$q_c \approx \frac{4A\rho g\omega\Lambda}{\rho g\Lambda + i\omega q_R} B_{00} N_0(\kappa_0 h); \tag{A12a}$$

$$p_c \approx \frac{4A\rho g\omega}{\rho g\Lambda + i\omega q_R} B_{00} N_0(\kappa_0 h). \tag{A12b}$$

Reference

[1] Falcão A F de O. Wave energy utilization: A review of the technologies. Renewable and Sustainable Energy Reviews, 2010, 14(3): 899-918.

[2] Heath T V. A review of oscillating water columns. Philosophical Transactions of the Royal Society London, Series A: Mathematical, Physical and Engineering Sciences, 2012, 370(1959): 235-245.

[3] Wang D J, Katory M, Li Y S. Analytical and experimental investigation on the hydrodynamic performance of onshore wave-power devices. Ocean Engineering, 2002, 29(8): 871-885.

[4] Koo W, Kim M H. Nonlinear time-domain simulation of a land-based oscillating water column. Journal of waterway, port, coastal, and ocean engineering, 2010, 136(5): 276-285.

[5] Luo Y Y, Nader J R, Cooper P, et al. Nonlinear 2D analysis of the efficiency of fixed oscillating water column wave energy converters. Renewable energy, 2014, 64: 255-265.

[6] Ning D Z, Zhao X L, Zhao M, et al. Analytical investigation of hydrodynamic performance of a dual pontoon WEC-type breakwater. Applied Ocean Research, 2017, 65: 102-111.

[7] Vyzikas T, Deshoulières S, Barton M, Ciroux O, Greaves D, Simmonds D. Experimental investigation of different geometries of fixed oscillating water column devices. Renewable Energy, 2017, 104: 248-258.

[8] Evans D V, Porter R. Efficient calculation of hydrodynamic properties of OWC-Type devices. Journal of Offshore Mechanics and Arctic Engineering, 1997, 119(4): 210-218.

[9] Gomes R P F, Henriques J C C, Gato L M C, Falcão A F O. Hydrodynamic optimization of an axisymmetric floating oscillating water column for wave energy conversion. Renewable Energy, 2012, 44: 328-339.

[10] Elhanafi A, Macfarlane G, Fleming A, Leong Z. Experimental and numerical investigations on the intact and damage survivability of a floating–moored oscillating water column device. Applied Ocean Research, 2017, 68: 276-292.

[11] Falcão A F de O. Wave-power absorption by a periodic linear array of oscillating water columns. Ocean Engineering, 2002, 29(10): 1163-1186.

[12] Nader J R, Zhu S P, Cooper P, Stappenbelt B. A finite-element study of the efficiency of arrays of oscillating water column wave energy converters. Ocean Engineering, 2012, 43: 72-81.

[13] Nihous G C. Wave power extraction by arbitrary arrays of non-diffracting oscillating water columns. Ocean Engineering, 2012, 51: 94-105.

[14] Rezanejad K, Bhattacharjee J, Guedes Soares C. Analytical and numerical study of dual-chamber oscillating water columns on stepped bottom. Renewable Energy, 2015, 75: 272-282.

[15] Konispoliatis D N, Mavrakos S A. Hydrodynamic analysis of an array of interacting free-floating oscillating water column (OWC's) devices. Ocean Engineering, 2016, 111: 179-197.

[16] He F, Leng J, Zhao X Z. An experimental investigation into the wave power extraction of a floating box-type breakwater with dual pneumatic chambers. Applied Ocean Research, 2017, 67: 21-30.

[17] Ning D Z, Zhou Y, Zhang C W. Hydrodynamic modeling of a novel dual-chamber OWC wave energy converter. Applied Ocean Research, 2018, 78:180-191.

[18] Vijayakrishna Rapaka E, Natarajan R, Neelamani S. Experimental investigation on the dynamic response of a moored wave energy device under regular sea waves. Ocean Engineering, 2004, 31(5): 725-743.

[19] Martins-Rivas, H, Mei C C. Wave power extraction from an oscillating water column at the tip of a breakwater. Journal of Fluid Mechanics, 2009, 626: 395-414.

[20] He F, Huang Z, Law A W K. An experimental study of a floating breakwater with asymmetric pneumatic chambers for wave energy extraction. Applied energy, 2013, 106: 222-231.

[21] Muliawan M J, Karimirad M, Gao Z, Moan T, Extreme responses of a combined spar-type floating wind turbine and floating wave energy converter (STC) system with survival modes, Ocean Engineering, 2013, 65: 71–82.

[22] Michailides C, Gao Z, Moan T. Experimental and numerical study of the response of the offshore combined wind/wave energy concept SFC in extreme environmental conditions. Marine

878 Structures, 2016, 50:35-54.
879 [23] Peiffer A, Roddier D, Aubault A. Design of a point absorber inside the WindFloat structure. In
880 Proceedings of the 30th International Conference on Ocean, Offshore and Arctic Engineering,
881 Rotterdam, The Netherlands, June 19–24, 2011.
882 [24] Ren N X, Gao Z, Moan T, Wan L. Long-term performance estimation of the Spar-Torus-
883 Combination (STC) system with different survival modes. Ocean Engineering, 2015, 108: 716-728.
884 [25] Wan L, Gao Z, Moan T, Lugni C. Experimental and numerical comparisons of hydrodynamic
885 responses for a combined wind and wave energy converter concept under operational conditions,
886 Renewable Energy, 2016, 93: 87–100.
887 [26] Aubault A., Alves M., Sarmento A, Roddier D, Peiffer A. Modeling of an oscillating water
888 column on the floating foundation WindFloat. In: Proceedings of the 30th International Conference
889 on Ocean, Offshore and Arctic Engineering, Rotterdam, The Netherlands, June 19–24, 2011.
890 [27] Perez-Collazo C, Greaves D, Iglesias G. Hydrodynamic response of the WEC sub-system of a
891 novel hybrid wind-wave energy converter. Energy Conversion and Management, 2018, 171: 307-
892 325.
893 [28] Perez-Collazo C, Pemberton R, Greaves D, Iglesias G. Monopile-mounted wave energy
894 converter for a hybrid wind-wave system. Energy Conversion and Management, 2019, 199: 111971.
895 [29] Michele S, Renzi E, Perez-Collazo C, Greaves D, Iglesias G. Power extraction in regular and
896 random waves from an OWC in hybrid wind-wave energy systems. Ocean Engineering, 2019, 191:
897 106519.
898 [30] Sarmiento J, Iturrioz A, Ayllón V, Guanche R, Losada I J. Experimental modelling of a multi-
899 use floating platform for wave and wind energy harvesting. Ocean Engineering, 2019, 173: 761-
900 773.
901 [31] Zhou Y, Ning D Z, Shi W, Johanning L, Liang D F. Hydrodynamic investigation on an OWC
902 wave energy converter integrated into an OWT monopile, Coastal Engineering, 2020, 103731.
903 [32] Michailides C, Gao Z, Moan T, Experimental study of the functionality of a semisubmersible
904 wind turbine combined with flap type wave energy converters. Renewable Energy, 2016, 93: 675–
905 690.
906 [33] Li Q Y, Michailides C, Gao Z, Moan T. A comparative study of different methods for predicting
907 the long-term extreme structural responses of the combined wind and wave energy concept

908 semisubmersible wind energy and flap-type wave energy converter. Proceedings of the Institution
909 of Mechanical Engineers, Part M: Journal of Engineering for the Maritime Environment, 2018,
910 232(1): 85-96.
911 [34] Wang X F, Zeng X W, Li X Y, Li J L. Investigation on offshore wind turbine with an innovative
912 hybrid monopile foundation: An experimental based study. Renewable Energy, 2019, 129-141.
913 [35] Sarmento A J N A, Falcão A F O. Wave generation by an oscillating surface-pressure and its
914 application in wave-energy extraction. Journal of Fluid Mechanics, 1985, 150: 467-485.
915 [36] Sheng W A, Alcorn R, Lewis A. On thermodynamics in the primary power conversion of
916 oscillating water column wave energy converters. Journal of Renewable and Sustainable Energy,
917 2013, 5(2): 023105.
918 [37] Cruz J. Ocean Wave Energy. 2008, Springer, Berlin, Heidelberg, Germany.
919 [38] Teng B, Eatock Taylor R. New higher-order boundary element method for wave
920 diffraction/radiation. Applied Ocean Research, 1995, 17(2): 71-77.
921 [39] Falnes J, Mciver P. Surface wave interactions with systems of oscillating bodies and pressure
922 distributions. Applied Ocean Research, 1985, 7(4): 225-234.
923 [40] Jonkman J, Butterfield S, Musial W, Scott G. Definition of a 5-MW Reference Wind Turbine
924 for Offshore System Development. Technical Report NREL/TP-500-38060, National Renewable
925 Energy Laboratory, USA, 2009.
926 [41] Deng Z Z, Huang Z H, Law A W K. Wave power extraction by an axisymmetric oscillating-
927 water-column converter supported by a coaxial tube-sector-shaped structure. Applied Ocean
928 Research, 2013, 42: 114-123.
929 [42] Goda Y. Statistical variability of sea state parameters as a function of wave spectrum. Coastal
930 Engineering in Japan, 1988, 31(1): 39-52.
931 [43] Ren N X, Ma Z, Fan T H, Zhai G J, Ou J P. Experimental and numerical study of hydrodynamic
932 responses of a new combined monopile wind turbine and a heave-type wave energy converter under
933 typical operational conditions. Ocean Engineering, 2018, 159: 1-8.